Global and Planetary Change 171 (2018) 18–47

Contents lists available at ScienceDirect

Global and Planetary Change

journal homepage: www.elsevier.com/locate/gloplacha

Research article

Refining the thermal structure of the European lithosphere by inversion of subsurface temperature data

Jon Limberger[a,*], Jan-Diederik van Wees[a,b], Magdala Tesauro[c], Jeroen Smit[a], Damien Bonté[a], Eszter Békési[a], Maarten Pluymaekers[b], Maartje Struijk[b], Mark Vrijlandt[b], Fred Beekman[a], Sierd Cloetingh[a]

[a] Utrecht University, Department of Earth Sciences, PO Box 80021, Utrecht 3508 TA, the Netherlands
[b] TNO, PO Box 80015, Utrecht 3508 TA, the Netherlands
[c] Università degli Studi di Trieste, via Weiss 1, Palazzina C, Trieste 34127, Italy

ARTICLE INFO

Editor: Prof. Sierd Cloetingh

Keywords:
3D temperature
Heat flow
Geothermal
(Bulk) thermal conductivity
Radiogenic heat generation
Ensemble smoother multiple data assimilation
Lithosphere
Europe

ABSTRACT

We present an updated thermal model of the European lithosphere based on a new stochastic modeling work flow. We developed this work flow to estimate subsurface temperatures from site- to regional-scale, up to the depth of the lithosphere-asthenosphere boundary (LAB). Our model is composed of four layers, consisting of sediments, upper crust, lower crust and lithospheric mantle. We asigned thermal properties, including radiogenic heat production and temperature- and pressure-dependent bulk thermal conductivity on the base of broad-scale lithological variation within the European crust. We corrected thermal properties with a 1D steady-state temperature approximation, assuming only vertical heat flow. Using these corrected thermal properties, we calculated the 3D thermal field with a conjugate-gradient method, assuming fixed temperatures at the surface and at the base of the lithosphere. To obtain more robust results for our thermal model, we applied data assimilation, aiming at consistency between temperature and heat flow observations and tectonic model predictions. We used an Ensemble Smoother Multiple with Data Assimilation (ES-MDA) method to update prior estimates of thermal properties and the thermal field with temperature data. We calibrated our European thermal model with available regional thermal models due to the present lack of a unified dataset with public borehole temperature measurements. A large dichotomy is observed in the model along the Trans-European Suture Zone (TESZ). Northeast of the TESZ, geothermal gradients up to 10 km depth are mainly below 20 °C km^{-1}. Southwest of the TESZ, gradients range from 20 °C km^{-1} near the Adriatic coast to more than 50 °C km^{-1} in volcanically and tectonically active regions. We show that the large scale thermal structure is locally and regionally perturbed by non-conductive heat transfer and affected by transient effects.

1. Introduction

This paper shows how we implemented a stochastic work flow to model temperatures and associated thermal properties on a European-scale up to the depth of the lithosphere. The work flow consists of three modules: the first module applies a multi-1D method to populate the model with *a priori* thermal properties; the second module uses these properties to calculate the *a priori* 3D thermal field; and the final module consists of a sequential stochastic modelling tool that returns the *a posteriori* thermal field and corresponding *a posteriori* thermal properties. We calibrated our model using a compilation of temperature models based on temperature measurements (Limberger et al., 2014). To obtain a best fit with the available data, we used an Ensemble Smoother with Multiple Data Assimilation (ES-MDA) method from Emerick and Reynolds (2013). For each data assimilation sequence, multiple iterations were performed using an inflated covariance matrix of the observation errors. Each iteration returned an ensemble, based on a predefined number of model runs where one or more variables were varied using Monte Carlo Sampling, following the prior probability distributions and variograms of the model parameters.

For our European model, we used ES-MDA to sequentially vary the lower thermal boundary condition, radiogenic heat production in the upper crust, and bulk thermal conductivity within the upper 15 km of the model. Temperature observations used for this calibration do not solely reflect steady-state conductive heat transfer. In many regions within Europe, transient effects and non-conductive heat flow affect

* Corresponding author.
E-mail address: J.Limberger@uu.nl (J. Limberger).

https://doi.org/10.1016/j.gloplacha.2018.07.009
Received 11 July 2017; Received in revised form 19 April 2018; Accepted 18 July 2018
Available online 27 July 2018
0921-8181/

these observations. We discuss observed temperature variations within the upper crust (including sedimentary basins) and give an overview on the effect of differences in lithosphere structure, thermal properties, convective fluid flow and tectonic processes. An improved understanding of the thermal state of the European lithosphere will aid in geothermal resource assessments (e.g. Limberger et al., 2014, 2018).

Significant amount of work has been done on understanding the thermal structure of the European lithosphere (e.g. Cermak, 1993; Artemieva et al., 2006; Tesauro et al., 2009). However, this previous work largely focused on understanding the deeper thermal structure, not so well constrained by thermal data in sedimentary basins and without taking into account data assimilation techniques. We refer to the relevance of our work in relation to previous studies in the respective sections below.

2. Model geometry and a priori properties

2.1. Deep crustal structure and composition

For the European subsurface, there are various data sources for the deep crustal structure and composition. We adopted the EuCrust-07 model from Tesauro et al. (2008, 2009) as a layered structure of the lithosphere (Figs. 1a, 2a, 3a and 4a), with different domains within the upper and lower crust (Figs. 2b and 3b). The model volume extends over mainland Europe and ranges up to 100 km depth. We discretized the model volume at a 20 km resolution in horizontal direction. To keep the number of cells for such a large model and a large set of observations (Section 3.5) manageable for data assimilation, we used two vertical resolutions: 0.25 km was adopted for the top 5 km of the model and 0.5 km for the deeper parts.

We used a lithological-interpretation-approach to assign properties to the layers (Tables 1 to 5). Based on these layers and their corresponding domains, we defined lithological compositions or lithofacies (Tables 2 and 5) that we refer to as lithotypes. Each lithotype consists of a single lithology or a mixture of lithologies. The properties that we assigned to each lithology (Tables 3 to 5) are derived from existing databases and catalogues (Hantschel and Kauerauf, 2009; Bär et al., 2016). We defined the top of our model based on the topography of the ETOPO1 1 Arc-Minute Global Relief Model of Amante and Eakins (2009).

2.2. Lithological variability in sediments

The variability in lithology and effects of compaction of sediments are significant factors for determining thermal properties. A detailed structure and compositional input for sedimentary basins is of key importance for thermo-mechanical models of deep portions of basins and crust (e.g. Ziegler et al., 1995, 1998; van Wees and Beekman, 2000).

To date, no unifying dataset exists in Europe of the detailed crustal structure, sedimentary infill of basins and faults, while at regional scale such data are generally available for selected regions. The present lack of a unified dataset for Europe led us to use a single layer for the sediments based on the sediment thickness from Tesauro et al. (2008). Surface geology is, however, mapped in detail and globally available (e.g. portal.onegeology.org). We therefore spatially divided the sedimentary layer of our model into different domains based on the Global Lithology Map (GLiM) from Hartmann and Moosdorf (2012). We chose generalized sedimentary lithotypes (Fig. 1b) for which we assumed specific lithology mixtures described in Table 2. Based on these generalized sedimentary lithotypes of the surface geology we defined our sedimentary domains.

2.3. Thermal properties

For the *a priori* thermal properties we followed a similar approach as described in Limberger et al. (2017), but in this study we used the 1D method to populate each model grid cell before calculating the 3D thermal field. For a European-scale model, choosing a single value for thermal conductivity and heat generation a priori for each layer is problematic, as single values would have to encompass the probable mixtures of pure lithologies as well as likely thermal and compaction effects.

Instead, we used the sedimentary and crustal lithotypes discussed in the previous paragraphs as a base for choosing lithology mixtures with associated reference thermal properties based on basin modeling best practices. This is a more practical approach that separates more clearly between our a priori assumptions on the thermal properties and our results after calibrating the model with ES-MDA.

2.3.1. Thermal conductivity

Throughout our model, thermal conductivity was corrected for temperature and pressure conditions, resulting in a collection of 1D thermal conductivity profiles:

$$k(z) = \begin{cases} k_{SED}(z) & : z \geq 0 \vee z < z_{topUC} \\ k_{UC}(z) & : z \geq z_{topUC} \vee z < z_{topLC} \\ k_{LC}(z) & : z \geq z_{topLC} \vee z < z_{topLM} \\ k_{LM}(z) & : z \geq z_{topLM} \vee z < z_{LAB} \end{cases} \quad (1)$$

where $k_{SED}(z)$, $k_{UC}(z)$, $k_{LC}(z)$ and $k_{LM}(z)$ are thermal conductivities [$W\,m^{-1}\,K^{-1}$] as a function of depth z [m] for the sediments, upper crust, lower crust and lithospheric mantle, respectively. z_{topUC}, z_{topLC}, z_{topLM} and z_{LAB} are the depths [m] of the top of the upper crust, lower crust, lithospheric mantle and the lithosphere-asthenosphere boundary, respectively. For the different lithotypes in the sedimentary layer, a bulk matrix thermal conductivity k_m was used, consisting of one or more lithological components, corrected for the in situ temperature following Sekiguchi (1984):

$$k_m(z) = 358 + (1.0227 k_i^{20} - 1.882)\left(\frac{1}{T + 273} - 0.00068\right) + 1.84 \quad (2)$$

where k_i^{20} is the matrix thermal conductivity [$W\,m^{-1}\,K^{-1}$] at room temperature (20 °C) and T is the temperature [°C]. For each lithological component, the horizontal matrix conductivity was calculated from k_m using anisotropy factors for different lithologies (Table 3). For shales and carbonates, k_m was also corrected for the change in anisotropy with increasing compaction (Hantschel and Kauerauf, 2009). The bulk density of sediments depends on the amount of mechanical compaction that has occured. For our sediment layer we based the bulk density on the weighted average of the matrix density of the mixed lithologies (Table 4). For the upper crust, lower crust, and lithospheric mantle we assumed fixed densities (Table 5).

We assumed pure water for the pore fluid with hydrostatic conditions throughout the model. The effective vertical stress σ_v' [MPa] was obtained by subtracting the hydrostatic pressure from the lithostatic stress. For the lithostatic stress σ_{litho}, we chose the vertical stress as the maximum principle stress. We calculated σ_{litho} by multiplying the gravitational acceleration g with the integral of the density ρ over a given depth interval z:

$$\sigma_{litho} = \sigma_o + g \int_0^z \rho(z) dz. \quad (3)$$

Then the function of σ_v' with depth z [m] was used to calculate compaction curves based on Schneiders relationship, which is an extended version of Athy's Effective Stress law for compaction (Athy, 1930; Schneider et al., 1996). For each lithotype, the depositional porosity defined by Hantschel and Kauerauf (2009) was adopted as surface porosity. These surface porosities were then combined with the corresponding compaction coefficients to calculate the porosity at each depth.

For each lithology in the mixture, the bulk thermal conductivity was

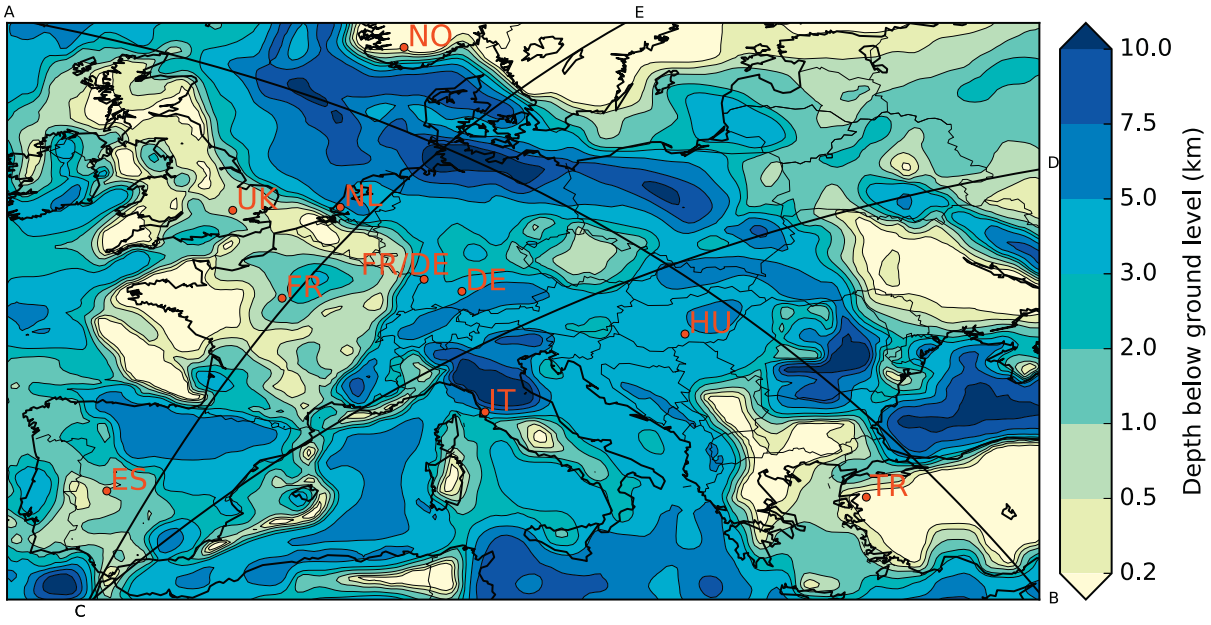

(a)

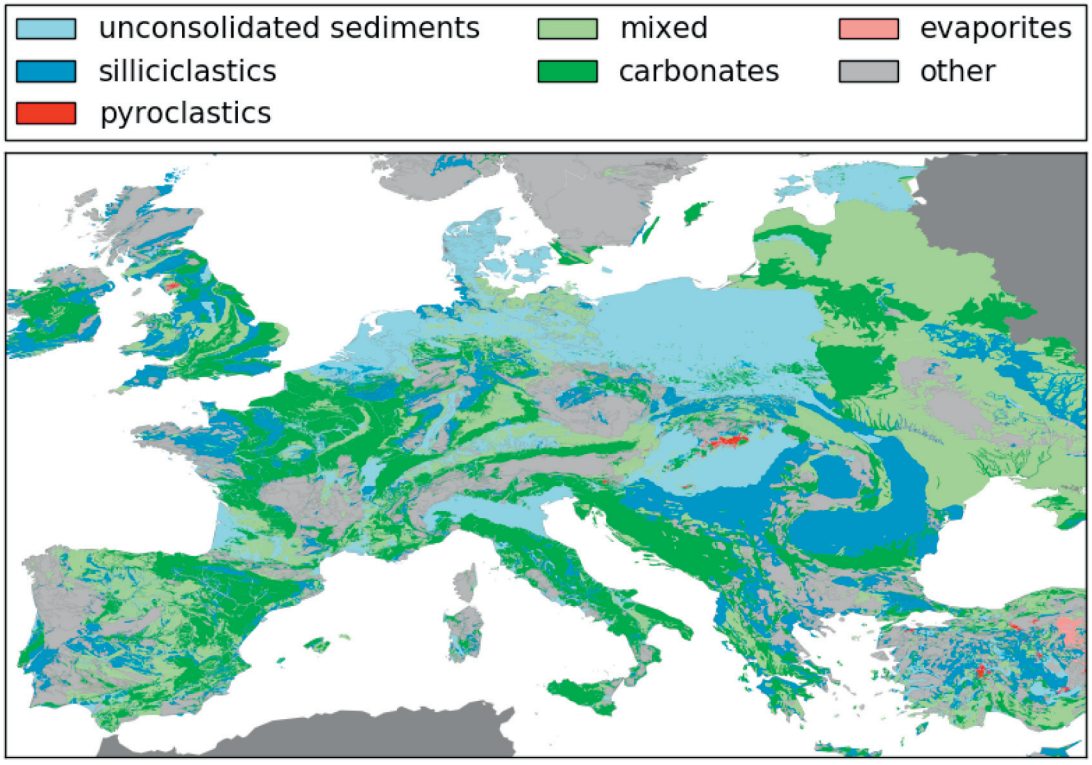

(b)

Fig. 1. (a) Depth to the base of the sediments after Tesauro et al. (2008). NO = Norway, UK = United Kingdom, NL = West Netherlands basin in the Netherlands, FR = Paris Basin in France, FR/DE = Upper Rhine Graben part of the European Cenozoic Rift System (ECRIS), DE = Molasse Basin in Germany, HU = Pannonian Basin in Hungary, IT = Lardarello geothermal region in Tuscany, Italy, TR = Western Anatolia in Turkey, ES = Spanish Central System. (b) Sediment lithotypes after Hartmann and Moosdorf (2012) (see Table 2).

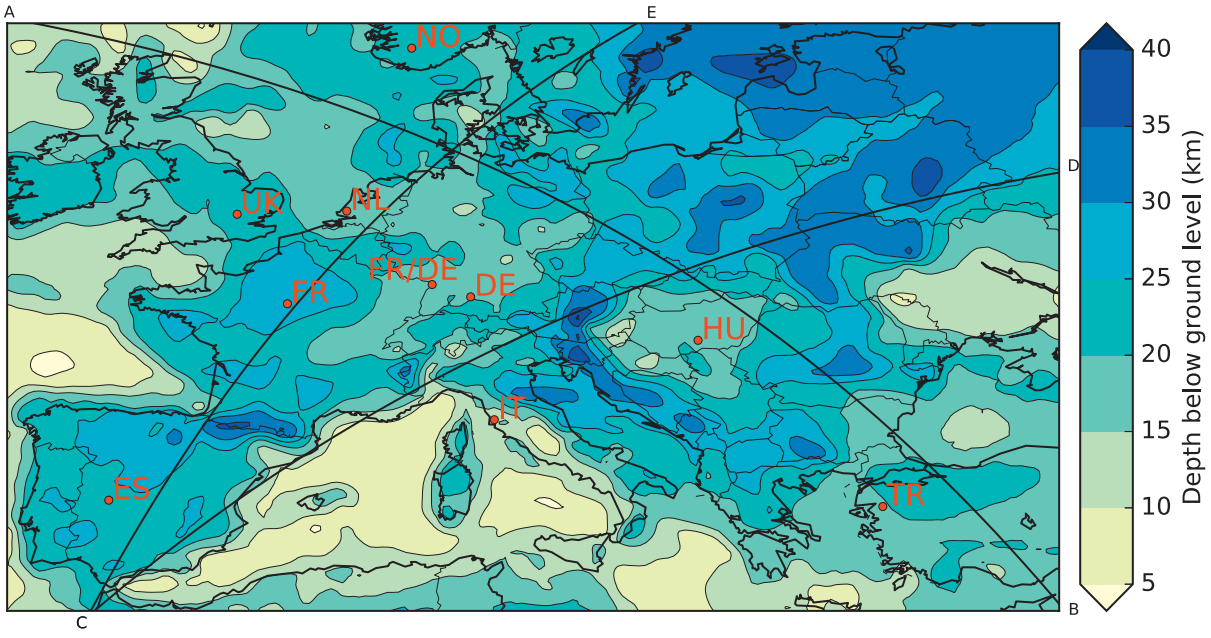

(a)

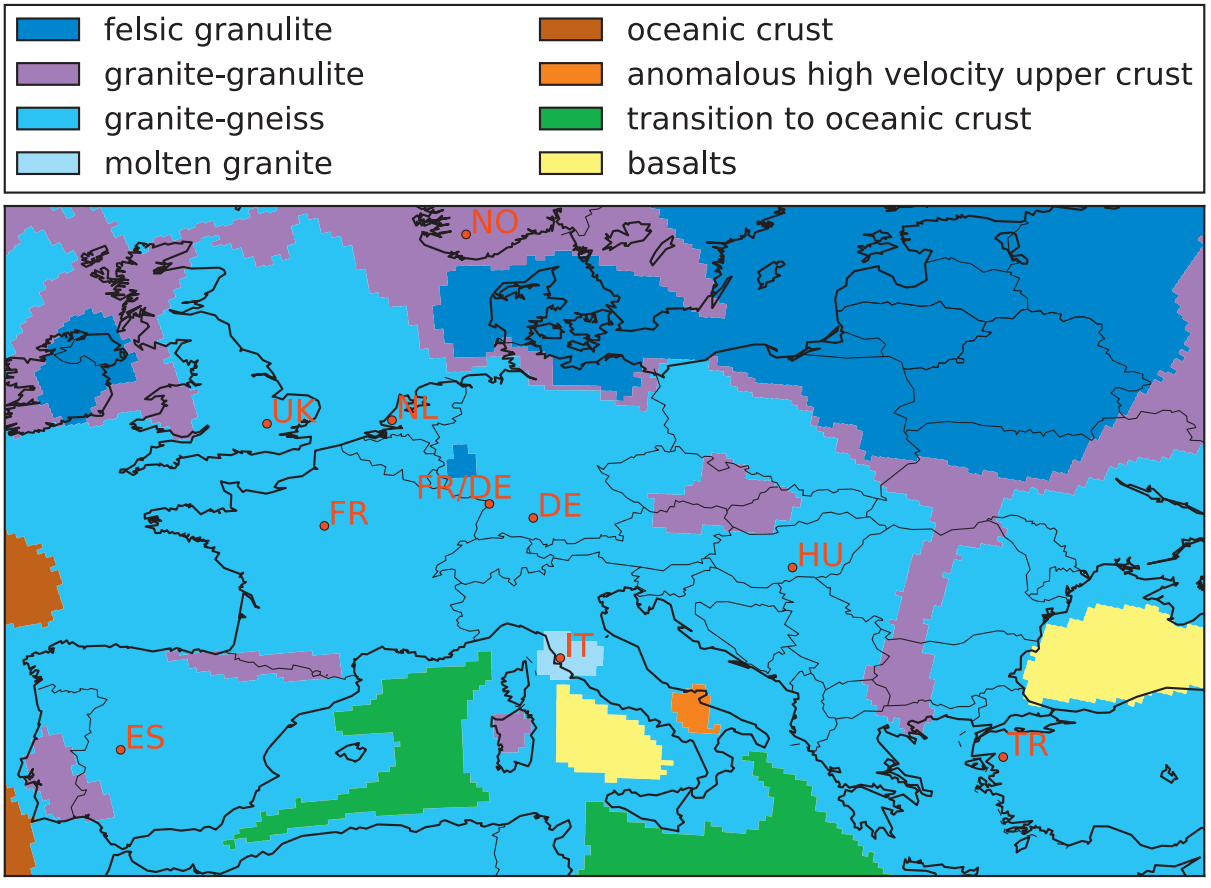

(b)

Fig. 2. (a) Depth to the base of the upper crust after Tesauro et al. (2008). (b) Upper crust lithotypes after Tesauro et al. (2009) (see Table 5).

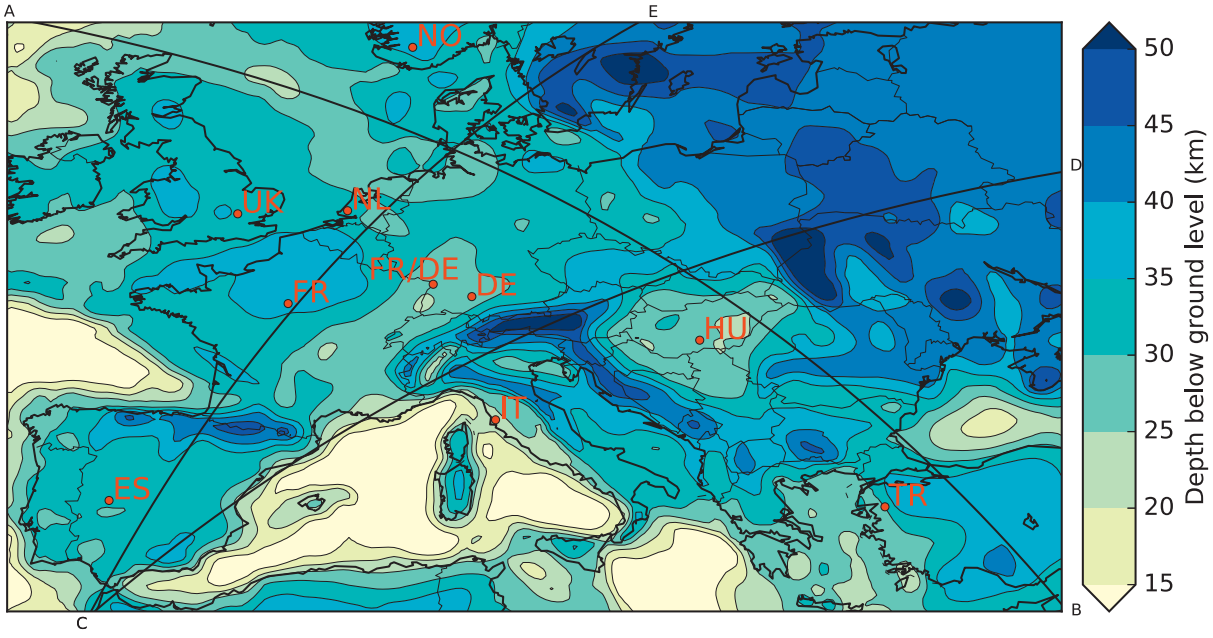

(a)

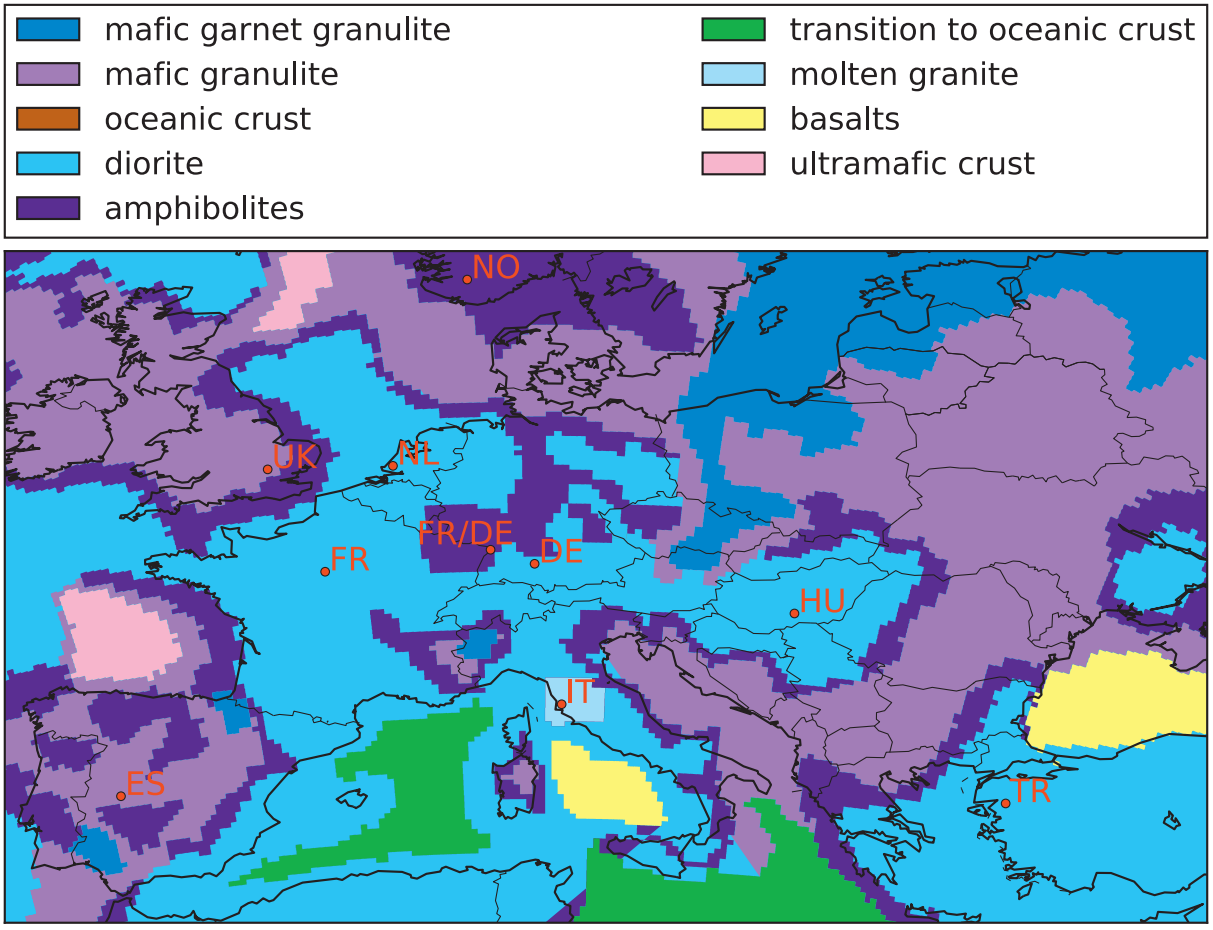

(b)

Fig. 3. (a) Depth to the base of the lower crust after Tesauro et al. (2008). (b) Lower crust lithotypes after Tesauro et al. (2009) (see Table 5).

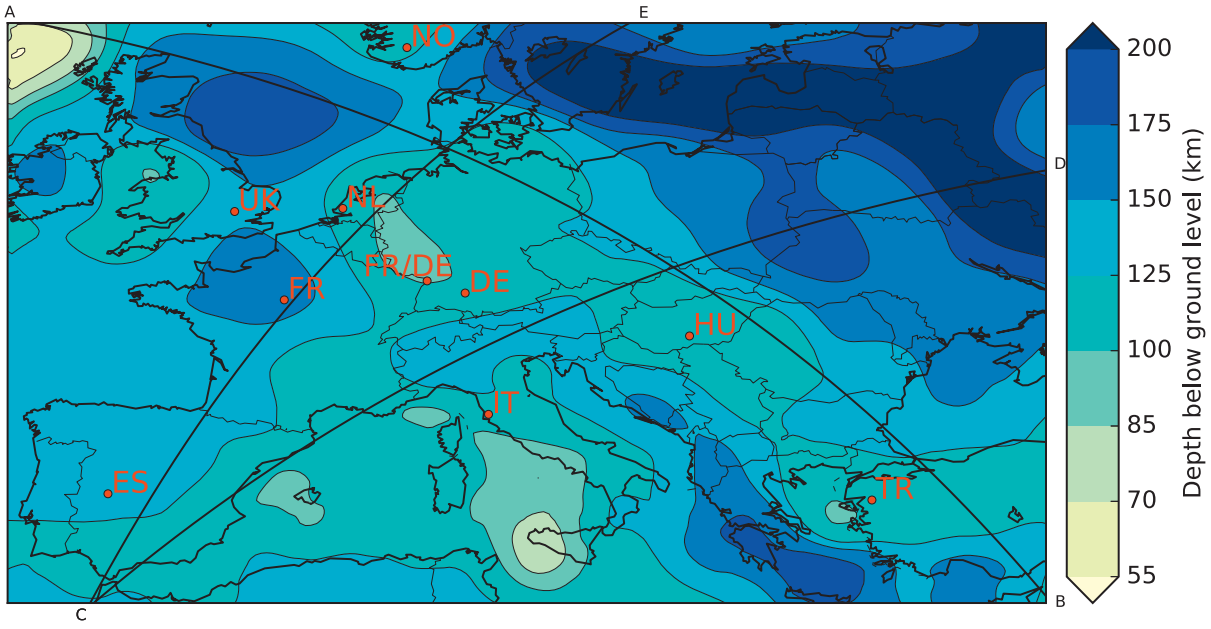

(a)

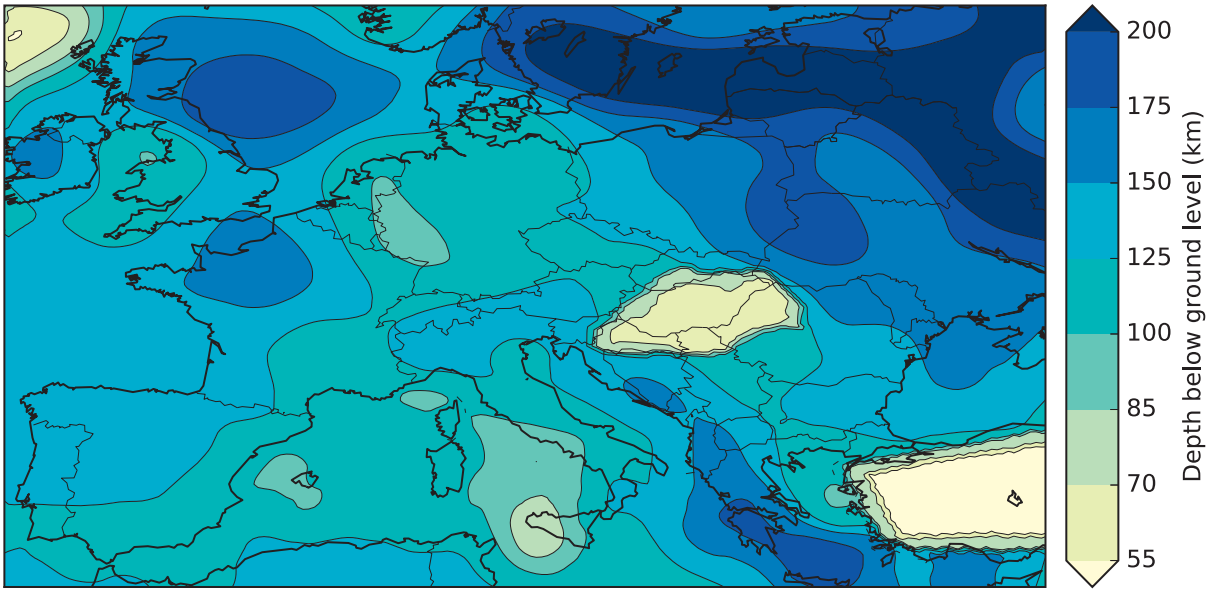

(b)

Fig. 4. (a) Thermal lithosphere thickness (LAB) after Tesauro et al. (2009). (b) Thermal lithosphere thickness adjusted for the Pannonian Basin and western Anatolia (see text).

Table 1
A priori (bulk) thermal conductivity and radiogenic heat generation per layer. Ranges of k and A indicate the range of the uncorrected base value.

Layer	k [W m^{-1} K^{-1}]	Range	A [μ W m^{-3}]	Range
Sediments	Variable: matrix values per lithotype (mixed lithologies from Table 2) dependent on compaction and temperature (Eq. (2))	1.2–2.2	Variable: matrix values per lithotype (mixed lithologies from Table 2) and bulk values dependent on compaction	0.40–2.70
Upper crust	Variable: pressure and temperature dependent (Eq. (6))	1.7–2.9	Constant: depending on lithotype (Table 5)	0.00–3.33
Lower crust	Variable: pressure and temperature dependent (Eq. (7))	~2.6	Constant: depending on lithotype (Table 5)	0.00–0.85
Lithospheric mantle	Variable: pressure and temperature dependent (Eq. (8))	2.7–3.5	Constant: depending on lithotype (Table 5)	0.02

Table 2
Sedimentary lithotypes based on the surface geology (Fig. 1b) and our assumptions on lithology mixtures for each lithotype.

#	Lithotype[1]	Lithology mixtures[2]
1	Unconsolidated	25% conglomerate typical; 25% sandstone typical; 25% siltstone organic rich typical; 25% shale typical
2	Unconsolidated (coarse)	34% sandstone typical; 33% conglomerate typical; 33% shale typical
3	Unconsolidated (fine)	34% sandstone typical; 33% siltstone organic rich typical; 33% shale typical
4	Siliciclastic	50% siltstone organic rich typical; 30% sandstone typical; 20% shale typical
5	Siliciclastic (coarse)	50% sandstone typical; 30% siltstone organic rich typical; 20% shale typical
6	Siliciclastic (fine)	75% shale typical; 25% siltstone organic rich typical
7	Pyroclastics	75% felsic tuff; 25% basaltic tuff
8	Mixed sediments	50% (4) siliciclastic; 50% (11) carbonates
9	Mixed sediments (coarse)	50% (5) siliciclastic (coarse); 50% (11) carbonates
10	Mixed sediments (fine)	50% (6) siliciclastic (fine); 50% (11) carbonates
11	Carbonates	25% ooid limestone; 25% dolomite typical; 25% chalk typical; 25% marl
12	Evaporites	25% anhydrite; 25% chert; 25% gypsum; 25% halite
13	Other (e.g. offshore)	Constant

[1] (c.f. Hartmann and Moosdorf, 2012).
[2] (c.f. Hantschel and Kauerauf, 2009).

Table 3
Vertical matrix thermal conductivities at room temperature (20 °C) and anisotropy values to calculate the horizontal matrix thermal conductivity for the mixtures presented in Table 2 based on lithologies from Hantschel and Kauerauf (2009).

#	k ($W m^{-1} K^{-1}$)	Anisotropy factor
1	2.30 & 3.95 & 2.01 & 1.25	1.05 & 1.15 & 1.71 & 1.60
2	3.95 & 2.30 & 1.25	1.15 & 1.05 & 1.60
3	3.95 & 2.01 & 1.25	1.15 & 1.71 & 1.60
4	2.01 & 3.95 & 1.25	1.71 & 1.15 & 1.60
5	3.95 & 2.01 & 1.25	1.15 & 1.71 & 1.60
6	1.25 & 2.01	1.60 & 1.71
7	2.60 & 1.90	1.17 & 1.17
8	Mixed: # 4 & # 11	
9	Mixed: # 5 & # 11	
10	Mixed: # 6 & # 11	
11	3.00 & 4.20 & 2.90 & 2.00	1.19 & 1.06 & 1.07 & 1.45
12	6.30 & 4.80 & 1.50 & 6.50	1.05 & 1.00 & 1.15 & 1.01
13	Constant: 2.00	1.00

Table 4
Matrix radiogenic heat production base values and densities for the mixtures presented in Table 2 based on lithologies from Hantschel and Kauerauf (2009).

#	A ($\mu W m^{-3}$)	ρ ($kg m^{-3}$)
1	0.85 & 0.70 & 0.96 & 2.03	2700 & 2720 & 2710 & 2700
2	0.70 & 0.85 & 2.03	2720 & 2700 & 2700
3	0.70 & 0.96 & 2.03	2720 & 2710 & 2700
4	0.96 & 0.70 & 2.03	2710 & 2720 & 2700
5	0.70 & 0.96 & 2.03	2720 & 2710 & 2700
6	2.03 & 0.96	2700 & 2710
7	1.56 & 0.43	2650 & 2900
8	Mixed: # 4 & # 11	
9	Mixed: # 5 & # 11	
10	Mixed: # 6 & # 11	
11	0.35 & 0.29 & 0.60 & 1.11	2740 & 2790 & 2680 & 2700
12	0.09 & 0.38 & 0.05 & 0.01	2970 & 2650 & 2320 & 2200
13	Constant: 1.10	Constant: 2700

obtained by taking the geometric mean of the bulk rock matrix thermal conductivity k_m [$W m^{-1} K^{-1}$] and the temperature-dependent pore fluid k_w [$W m^{-1} K^{-1}$]:

$$k_{bulk}(z) = k_m^{1-\phi} k_w^{\phi} \quad (4)$$

where ϕ is the porosity [0-1]. To take into account mixing between different lithologies within our sedimentary lithotypes listed in Tables 2 and 3, the harmonic mean of the different bulk thermal conductivities was taken. In this way, we obtained the bulk thermal conductivity of each lithotype at a given depth z within our sediment layer: $k_{SED}(z)$

Table 5
Crustal lithotypes with corresponding values used for density and a priori radiogenic heat generation.

#	Lithotype[1]	Lithology[2]	A ($\mu W m^{-3}$)	ρ ($kg m^{-3}$)
Sediments				
1–13	Table 2	Table 2	Table 4	Table 4
Upper crust				
1	Felsic granulite	Granite 1 Ga	1.00	2650
2	Granite-granulite	Granodiorite	1.20	2720
3	Granite-gneiss	Granite 500 Ma	1.50	2650
4	Molten granite	Granite 150 Ma	3.32	2650
5	Oceanic crust	Basalt	0.00	2870
6	Anomalous high velocity upper crust	Granite 1 Ga	1.00	2650
7	Transition to oceanic crust	Basalt	0.00	2870
8	Basalts	Basalt	0.00	2870
Lower crust				
1	Mafic garnet granulite	Amphibolite	0.36	2960
2	Mafic granulite	Amphibolite	0.36	2960
3	Oceanic crust	Basalt	0.00	2870
4	Diorite	Diorite	0.36	2900
5	Amphibolites	Amphibolite	0.36	2960
6	Transition to oceanic crust	Basalt	0.00	2870
7	Molten granite	Granite 150 Ma	0.85	2650
8	Basalts	Basalt	0.00	2870
9	Ultramafic crust	Ultramafics	0.00	3310
Lithospheric mantle				
1	Peritodite	Peridotite	0.02	3200

[1] (c.f. Tesauro et al., 2009).
[2] (c.f. Hantschel and Kauerauf, 2009).

[$W m^{-1} K^{-1}$]:

$$k_{SED}(z) = \left(\frac{n}{\frac{1}{k_{bulk1}} + [...] + \frac{1}{k_{bulkn}}} \right) \quad (5)$$

where n is the number of lithological components within a lithotype. We chose the harmonic mean over the geometric mean because it is better suited for horizontal layered systems such as the infill of sedimentary basins, which were encompassed in a single sedimentary layer in this study. To correct for the pressure dependence of thermal conductivity in the crust and lithospheric mantle (Eqs. (6) to (8)), the effective vertical stress and lithostatic pressure were assumed to be equal. For the upper and lower crust, temperature and pressure corrections from Chapman (1986) were used:

$$k_{UC}(z) = k_{iUC}^{0} \left(\frac{1 + c\sigma_v'}{1 + bT} \right) \quad (6)$$

$$k_{LC}(z) = k_{iLC}^{0}\left(\frac{1 + c\sigma_v'}{1 + bT}\right) \tag{7}$$

where k_i^0 is the thermal conductivity [W m^{-1} K^{-1}] at a temperature of 0 °C and at atmospheric pressure, b [K^{-1}] and c [Pa^{-1}] are constants, σ_v' is the effective vertical stress and T is the temperature [°C]. With increasing temperature, the contribution of the radiative component of the thermal conductivity increases compared to the lattice component (e.g. Hofmeister, 1999). This effect is especially relevant for the lithospheric mantle that consists mainly of olivine. We used Schatz and Simmons (1972) for the temperature-dependent radiative contribution $k_{rad}(T)$ and followed Xu et al. (2004) for the temperature- and pressure-dependent lattice thermal conductivity $k_{lat}^{25}(T, \sigma_v')$:

$$\begin{aligned} k_{LM}(z) &= k_{lat}^{25}(T, \sigma_v') + k_{rad}(T) \\ &= \sqrt{\frac{298}{T + 273}}(1 + 0.0032\sigma_v') + 0.368 \times 10^{-9}(T + 273)^3 \end{aligned} \tag{8}$$

where k_{lat}^{25} is the thermal conductivity [W m^{-1} K^{-1}] of olivine at a temperature of 25 °C and at atmospheric pressure, T is the temperature [°C] and σ_v' is the effective lithostatic stress [GPa].

2.3.2. Radiogenic heat generation

Fixed values for the radiogenic heat generation $A(z)$ [μW m^{-3}] were used throughout the lithosphere:

$$A(z) = \begin{cases} A_{SED}(z) = A_{bulk} & : z \geq 0 \vee z < z_{topUC} \\ A_{UC}(z) = A_{lithotype} & : z \geq z_{topUC} \vee z < z_{topLC} \\ A_{LC}(z) = A_{lithotype} & : z \geq z_{topLC} \vee z < z_{topLM} \\ A_{LM}(z) = 0.02 & : z \geq z_{topLM} \vee z < z_{LAB} \end{cases} \tag{9}$$

where A_{SED}, A_{UC}, A_{LC} and A_{LM} are the values of radiogenic heat generation for the sediments, upper crust, lower crust and lithospheric mantle, respectively. For the sedimentary layer, fixed values for the radiogenic heat generation A_{bulk} were used depending on the lithotype (Table 4). Bulk values of the radiogenic heat generation increase with depth for siliciclastic lithotypes, as porosity decreases exponentially with depth due to mechanical compaction leading to a larger amount of rock matrix relative to the pore volume. For most continental lithosphere, the relationship between the surface heat flow Q_0 [W m^{-2}] and A_{UC} follows the partition model of Pollack et al. (1977):

$$A_{UC} = \frac{rQ_0}{D_{UC}} \tag{10}$$

where r is a ratio [0-1] and D_{UC} is the thickness of the upper crust [m]. The ratio r in the partition model usually lies between 0.26-0.4 (e.g. Pollack et al., 1977; Hasterok and Chapman, 2011) for continental upper crust.

The problem with surface heat flow measurements is that they are often conducted at depths < 1 km inside wells, where paleoclimatic perturbations or groundwater flow can have a strong effect on the heat flow measurement (Beardsmore and Cull, 2001). Recent erosion can also lead to overestimation, while sedimentation can lead to underestimation (e.g. van Wees et al., 2009). Instead of relying on Q_0 to constrain A_{UC}, we assumed fixed values for A_{UC} based on our crustal lithotypes (see Figs. 2b and 3b and Table 5).

Radiogenic elements are more abundant in felsic rocks due to their lithophile behaviour during (partial) melting of the mantle and crust (Lachenbruch, 1970). To take this into account, we assumed higher heat production values for the upper and lower crust of continental lithotypes and low values for the transitional (continental-to-oceanic crust) and oceanic crust lithotypes (c.f. Vilà et al., 2010; Jaupart et al., 2016; Hasterok and Webb, 2017). The heat production within the lithospheric mantle was assumed to be homogenous (Table 5).

2.3.3. Temperature corrected thermal conductivity

Thermal conductivity is temperature dependent and requires correction. To this end, we initially estimated the temperature using a multi-1D steady-state approach to solve the heat equation (van Wees et al., 2009). A simple surface heat flow estimation was used for each 1D column based on layer thicknesses, base values of the thermal properties for all layers, and temperatures at the top and bottom of the model:

$$\begin{aligned} Q_0 \approx & \left[T_{LAB} - T_0 + \frac{1}{2}\left(\bar{A}_{SED}\frac{\Delta z_{SED}^2}{\bar{k}_{SED}} + \bar{A}_{UC}\frac{\Delta z_{LC}^2}{\bar{k}_{UC}} + \bar{A}_{LC}\frac{\Delta z_{LC}^2}{\bar{k}_{LC}} + \bar{A}_{LM}\frac{\Delta z_{LM}^2}{\bar{k}_{LM}} \right) \right. \\ & + \bar{A}_{SED}\Delta z_{SED}\frac{\Delta z_{UC}}{\bar{k}_{UC}} + (\bar{A}_{SED}\Delta z_{SED} + \bar{A}_{UC}\Delta z_{UC})\frac{\Delta z_{LC}}{\bar{k}_{LC}} \\ & \left. + (\bar{A}_{SED}\Delta z_{SED} + \bar{A}_{UC}\Delta z_{UC} + \bar{A}_{LC}\Delta z_{LC})\frac{\Delta z_{LM}}{\bar{k}_{LM}} \right] / \\ & \left[\frac{\Delta z_{SED}}{\bar{k}_{SED}} + \frac{\Delta z_{UC}}{\bar{k}_{UC}} + \frac{\Delta z_{LC}}{\bar{k}_{LC}} + \frac{\Delta z_{LM}}{\bar{k}_{LM}} \right] \end{aligned} \tag{11}$$

where Q_0 [W m^{-2}] is the surface heat flow, T_{LAB} the temperature [°C] at the lithosphere-asthenosphere boundary (LAB), T_0 the temperature [°C] at the surface, Δz is the layer thickness [m], and $\bar{k}$ and $\bar{A}$ are the averaged thermal conductivity [W m^{-1} K^{-1}] and radiogenic heat production [μW m^{-3}] values for each layer.

Each vertical column was divided in layers, 250 m thick up to 5 km depth and 500 m for the rest of the column to the base of the model. We used the initial temperature to correct the thermal conductivity and together with the calculated surface heat flow $Q(0)$ and radiogenic heat production $A(z)$, the temperature at each vertical interval was calculated:

$$T(z) = T_0 + \int_0^z \frac{Q(\zeta)}{k(\zeta)} d\zeta \tag{12}$$

where the heat flow was extrapolated downwards to obtain the heat flow as a function of depth, $Q(z)$ [W m^{-2}], by subtracting the integral of the radiogenic heat production from the surface heat flow between the surface and depth z:

$$Q(z) = Q_0 - \int_0^z A(\zeta) d\zeta \tag{13}$$

Since the calculated thermal conductivity was not entirely consistent with the initial surface heat flow and the lower boundary condition, we used a Newton-Raphson algorithm to ensure that after each iteration step, the surface heat flow was updated to honor the lower boundary condition. The geotherms were then recalculated using the updated heat flow, followed by the correction of the thermal conductivity. This process was repeated for each 1D column until convergence (temperature at the LAB = 1200 °C ± 0.1 °C) was reached. On our workstation, equipped with a 4th generation Intel Core i7 with 4 physical and 8 logical cores, 32GB of ram, and a 1TB Solid State Drive, the entire procedure lasts less than 5 minutes for the ~7 million cells of our model.

2.4. Boundary conditions and reference temperature data

2.4.1. Upper boundary condition: surface temperature

For the upper boundary condition we assumed fixed temperatures at the surface on data from the WorldClim-Global Climate Database from Hijmans et al. (2005). This data set contains mean surface temperatures from 24542 locations that represent the 1950-2000 time period.

2.4.2. Lower boundary condition: lithosphere-asthenosphere boundary

The lithosphere-asthenosphere boundary (LAB) is the transition between the lithosphere and asthenosphere. There are multiple definitions of the LAB that do not necessarily coincide (Artemieva, 2013), but the thermal LAB can be used as a lower boundary condition

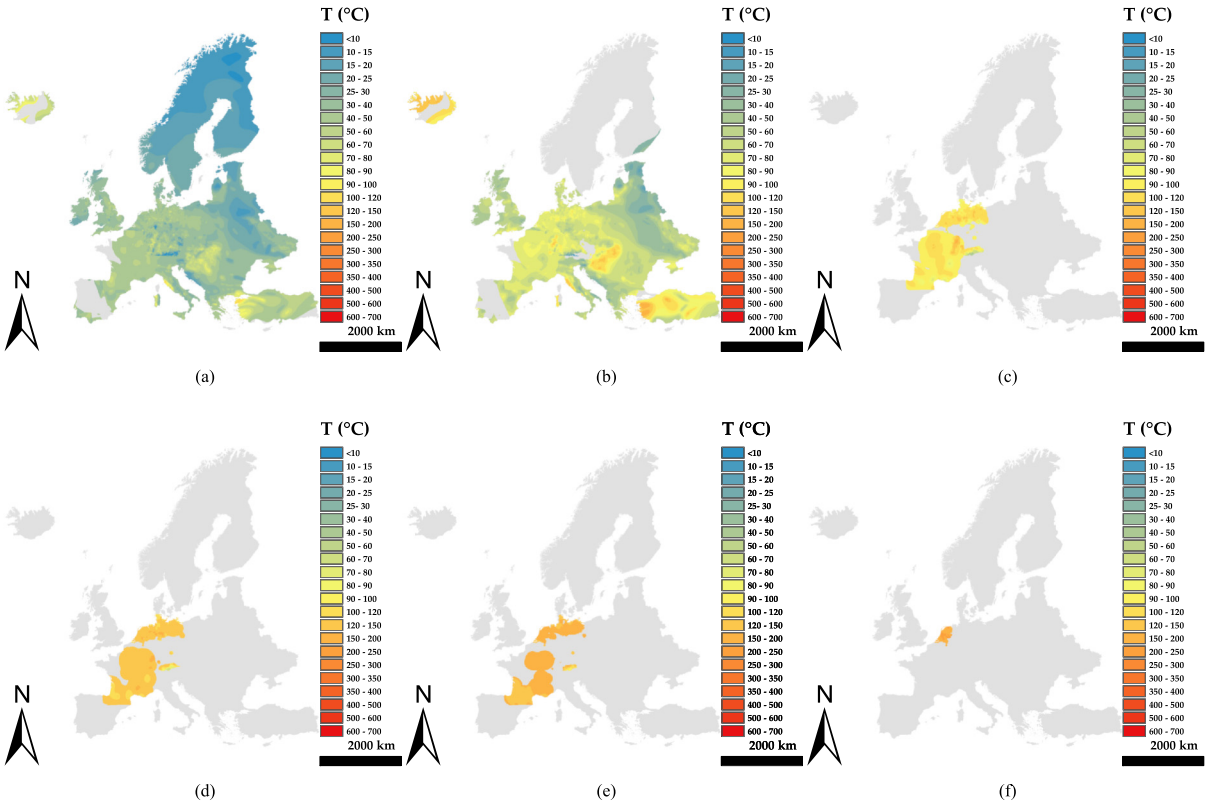

Fig. 5. (a–f) Input temperature maps at different depth levels (1–6 km) from Limberger et al. (2014) used for calibrating the model with ES-MDA. Temperatures of Ireland at 5 km (e) were not used as Jones et al. (2014) and Fullea et al. (2014) have shown that these are not reliable. We based the uncertainty of the sampled grid cells of our model on the amount of wells within each grid cell and the depth level (see Table 7).

(Dirichlet) for thermal models. The thermal LAB is defined as the transition between a predominantly conductive lithosphere and a predominantly convective asthenosphere. Because it is a transition rather than a sharp boundary, there is a significant uncertainty in LAB temperature (1200-1330 °C) and depth (Jaupart et al., 2007). For the depth of the LAB in this study, we used the model of Tesauro et al. (2009), where the LAB is defined as the depth of the 1200 °C isotherm (Fig. 4a). Tesauro et al. (2009) obtained the LAB by inversion of the tomography model of Europe from Koulakov et al. (2009). The filter used to smooth the velocity fields in Tesauro et al. (2009) is not able to preserve small-scale LAB variations for narrow tectonic structures such as the Pannonian Basin and western Anatolia. In this study, the thermal lithosphere thickness from Tesauro et al. (2009) (Fig. 4b) was therefore manually adjusted for the Pannonian Basin (c.f. Tari et al., 1999; Tašárová et al., 2009; Horváth et al., 2015; Lenkey et al., 2014; Békési et al., 2018) and western Anatolia (c.f. Angus et al., 2006; Kind et al., 2015).

2.4.3. Subsurface temperature data

Since 1970, several geothermal resource assessments of Europe have been conducted and their results have been published in a number of atlases commissioned by the European Union. These atlases include heat flow maps, locations of temperature measurements, and interpolated subsurface temperature maps of (parts of) Europe (Haenel, 1979; Haenel and Staroste, 1988). The most recent atlas commissioned by the EU was published in 2002 by Hurter and Haenel (2002) and is based on temperature data from Hurtig et al. (1992) but also includes newer temperature data. The temperature maps are based on Bottom Hole Temperature (BHT) and Drill Stem Test (DST) measurements. Although all the geographical coordinates of the wells are included and in some cases a measured heat flow is given, important information such as measurement depth, thermal conductivity or actual measured temperatures are lacking. All the geothermal atlases use ground level (GL) as datum for the depths. The depth notation used in this study is also relative to GL unless specified differently.

Several temperature maps have been digitized from these European geothermal atlases for the EU funded project GEOELEC (Dumas et al., 2013). From several national geological surveys, temperature models were received. These models cover (parts of) France, Germany, Ireland, the United Kingdom and the Netherlands. Apart from the UK, where only a map of the temperature at 1 km depth exists, these temperature models are relatively well constrained up to a depth of 2 km (Limberger et al., 2014). All of these models are based on BHT data, but the model approaches differ as well as corrections applied to the BHT data (Limberger et al., 2014). For this study, the digitized maps from the geothermal atlases and temperature maps from geological surveys were compiled into a temperature dataset (Fig. 5). Large parts were used for the data assimilation routine described in Section 3.

3. Forward model and data assimilation

3.1. Data assimilation procedure

Both the lower temperature boundary condition (LAB: Section 2.4.2 and Fig. 4b) and thermal properties of the layered structure (Tables 1 to 5) can be updated within reasonable bounds with a data assimilation procedure, using measured temperatures as target observations. However, measured temperatures should be critically evaluated and a weighting can be included reflecting the accuracy of the type of measurement (c.f. Rühaak et al., 2017). Outliers in the data can be caused by non-conductive thermal effects which may be related to heat advection and/or tectonic deformation. In our model, thermal conductivity and radiogenic heat generation are varied to obtain a better fit with the temperature observations, thereby acting as equivalent thermal properties encompassing both conductive and non-conductive

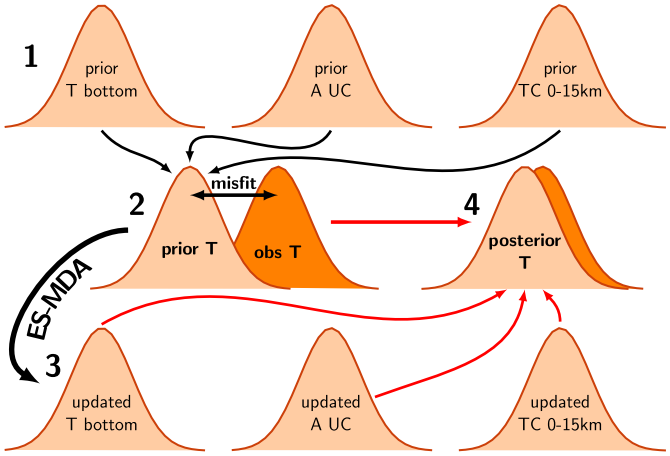

Fig. 6. Work flow of the data assimilation method used to update the temperature model and thermal properties. Uncertainties were assigned to main input parameters (1) including the temperature at the bottom of the model, radiogenic heat production (A), and thermal conductivity (k). In order to minimize the misfit between modeled and observed temperatures (2), the main parameters were varied using the Ensemble Smoother with Data Assimilation technique (3), resulting in an improved fit with temperature observations available (4). The model can be improved by varying all parameters all at once, but in this case we varied the parameters sequentially (see Table 6).

heat transfer. For deterministic forward models of the cooling plate model for oceanic crust, an equivalent thermal conductivity is occasionally used to approximate the combined thermal effect of conduction and convection (e.g. Morgan et al., 1987; Morgan and Chen, 1993; Schmelling and Marquart, 2014). Equivalent thermal conductivities are also used to estimate cooling rates of magmatic intrusions and to study ground deformation, taking into account both conductive and advective heat transport in porous rocks above the intrusion (e.g. Ascolese et al., 1993; Gaeta et al., 1998, 2003). For stochastic thermal models of sedimentary basins and crystalline basement, the use of equivalent thermal properties is relatively new (Békési et al., 2018). Although Jokinen (2000) briefly mentions that his inversion method could - with caution - be used for Phanerozoic stabilized continental crust, he does not mention the potential use of an equivalent thermal conductivity or equivalent heat production to approximate heat flow in dynamic regions that are thermally in non-steady state.

The data assimilation procedure we used is schematically outlined in Fig. 6, and is further explained in the following sections. The procedure starts with a prior physics-based forward model of predicted temperatures based on assumptions on boundary conditions and thermal properties. Subsequently, the model was parametrized using probability distributions, marking underlying uncertainties. Our predicted temperatures show a misfit with the observations, which in turn are also marked by uncertainty. Through an Ensemble Smoother Multiple Data Assimilation (ES-MDA) method (Emerick and Reynolds, 2013), the prior parameters of our model were updated to minimize the misfit between modeled and observed temperatures. Uncertainties were assigned to the observations and to the main parameters: the temperature of the lower boundary condition, radiogenic heat production, and thermal conductivity.

ES-MDA is an extension of the Ensemble Kalman filter (EnKF) for non-linear problems and was developed by Evensen (1994). For each data assimilation sequence, multiple iterations are performed using an inflated covariance matrix of the observation errors. Each iteration returns an ensemble that is based on a predefined number of model runs where one or more variables are varied (Monte Carlo Sampling) following prior probability distributions and variograms of the model parameters. The updated model parametrization and associated temperature model is called the posterior model.

3.2. Forward model

The forward thermal model solves the heat equation in an Eulerian model representation, where the model discretization is fixed:

$$\rho c_t \frac{\partial T}{\partial t} = \nabla \cdot (k_t \nabla T) + A \tag{14}$$

where T is temperature [K or °C], t is time [s], ρ is density [kg m^{-3}], c_t is specific heat capacity [J kg^{-1} K^{-1}], k_t is thermal conductivity [W m^{-1} K^{-1}], A is radiogenic heat production [W m^{-3}], ∇ is the nabla operator: $\left(\frac{\partial}{\partial x}, \frac{\partial}{\partial y}, \frac{\partial}{\partial z}\right)$ and $\cdot$ is the dot product. In this study, the left-hand side of Eq. (14) is zero because we only modeled steady– state conditions. We used a finite-difference approximation to solve Eq. (14) in 3D.

The relatively high vertical resolution and large vertical extent of our model, resulted in a large set of linear equations. These were solved by the Preconditioned Conjugate Gradient method (PCG), often used to solve the pressure equation for groundwater related problems (Guo and Langevin, 2002). The PCG-method is an indirect method to solve linear equations iteratively and is efficient for large problems.

We imposed the surface temperature and the temperature at the LAB (1200 °C) as Dirichlet boundary conditions for the top and bottom of the model, respectively, whereas the sides of the model were marked by a zero heat flux (Neumann) boundary condition. The finite-volume cells were marked by spatially variable thermal conductivity and radiogenic heat production as outlined in Section 2.

3.3. Ensemble smoother with multiple data assimilation

The goal of this inversion was to obtain information about the thermal state of our model from the set of observations. For each data assimilation sequence, multiple iterations N_a were performed using an inflated covariance matrix C_d of the observation errors. Each iteration returned an ensemble that was based on a predefined number of ensemble members N_e (model realizations) where one or more variables were varied with Monte Carlo Sampling, following the prior probability distributions and variograms of the model parameters (Table 6).

3.3.1. Definition and dimensions

$\boldsymbol{m}$	$n \times 1$	Model vector
$\boldsymbol{d_{obs}}$	$m \times 1$	Data vector
$\boldsymbol{\epsilon}$	$m \times m$	Data error vector
$\boldsymbol{C_m}$	$m \times m$	Model covariance
$\boldsymbol{C_d}$	$n \times n$	Data covariance
$\boldsymbol{G}$	$m \times n$	Linearized measurement operator matrix
$\mathscr{G}(\boldsymbol{m})$	$m \times 1$	Non-linear measurement operator (predicted value)

where n is the number of degrees of freedom in the model parameters, and m the number of observations. For most geophysical problems, n is much larger than m. With 35533 data points available and a total number of ~7 million cells in our model, the inverse problem is ill-posed and model solutions are therefore non-unique. An optimization routine was used for this model to minimize the cost function of the form:

$$\mathscr{J}(\boldsymbol{m}^a) = (\mathscr{G}(\boldsymbol{m}^a) - \boldsymbol{d_{obs}})^T \boldsymbol{C_d}^{-1} (\mathscr{G}(\boldsymbol{m}^a) - \boldsymbol{d_{obs}}) + (\boldsymbol{m}^a - \boldsymbol{m})^T \boldsymbol{C_m}^{-1} (\boldsymbol{m}^a - \boldsymbol{m}) \tag{15}$$

where $\boldsymbol{m}^a$ denotes the posterior (assimilated) model vector, based on prior model vector $\boldsymbol{m}$. Bold characters denote vectors and matrices when capitalized. The superscript ^{T} denotes the transposed value. Each model perturbation leads to variation away from the initial state of the model in order to fit the observations. The costs of each variation away from the initial state is dependent on the prior distribution of the parameters, and is balanced against the model misfits.

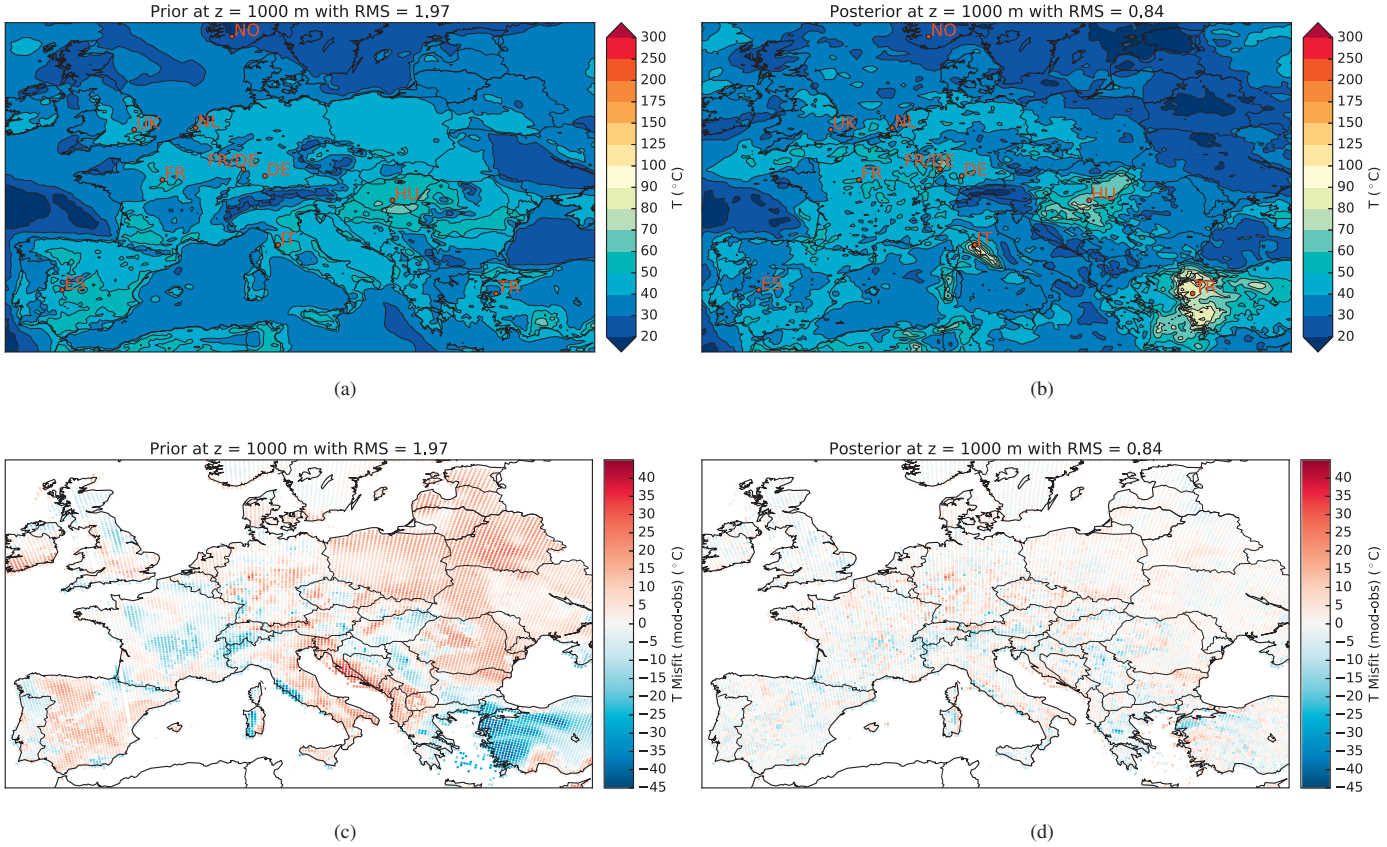

Fig. 7. (a) Temperatures of the prior (forward) 3D temperature model at 1000 m depth. (b) Temperatures of the posterior (calibrated) 3D temperature model at 1000 m depth. (c) Misfit of prior model (modeled temperatures minus observed temperatures). (d) Misfit of posterior model. NO = Norway, UK = United Kingdom, NL = West Netherlands basin in the Netherlands, FR = Paris Basin in France, FR/DE = Upper Rhine Graben part of the European Cenozoic Rift System (ECRIS), DE = Molasse Basin in Germany, HU = Pannonian Basin in Hungary, IT = Lardarello geothermal region in Tuscany, Italy, TR = Western Anatolia in Turkey, ES = Spanish Central System.

Table 6
Description of the three sequences used for the ES-MDA: for the first sequence the lower boundary condition was varied; in the second sequence the upper crustal (UC) radiogenic heat production; in the third sequence the (bulk) thermal conductivity of the top 15 km. For each data assimilation sequence, we specify the number of data assimilation iterations N_a, the number of ensemble members N_e (model runs for each iteration), the range or scaling factor for the allowed variation, the type of probability distribution, the variogram range (the radius of influence, 20 km = 1 cell), and the depth range or layers where a parameter was varied.

Parameter	Variation (shift/scale)	Range/scale factor	Distribution	Variogram range	Depth/layer/depth range
1: lower boundary condition: Na = 5 and Ne = 1000					
T	Shift	*T* −400, *T*, *T* +400	Triangular	Constant	100 km
2: radiogenic heat production: Na = 5 and Ne = 300					
A	Scale	0.1*A*, *A*, 3*A*	Triangular	300 km	UC
3: (bulk) thermal conductivity: Na = 5 and Ne = 300					
k	Scale	0.5*k*, *k*, 1.5*k*	Uniform	100 km	0–1 km
k	Scale	0.55*k*, *k*, 1.45*k*	Uniform	100 km	1–2 km
k	Scale	0.56*k*, *k*, 1.4*k*	Uniform	100 km	2–3 km
k	Scale	0.65*k*, *k*, 1.35*k*	Uniform	100 km	3–4 km
k	Scale	0.7*k*, *k*, 1.3*k*	Uniform	100 km	4–5 km
k	Scale	0.75*k*, *k*, 1.25*k*	Uniform	100 km	5–15 km

3.3.2. Ensemble smoother

In the ensemble smoother, the equation for the multiple data assimilation to minimize Eq. (15) can be written as (Emerick and Reynolds, 2013):

$$\boldsymbol{m}_j^a = \boldsymbol{m}_j + \widehat{\boldsymbol{C}}_{md}(\widehat{\boldsymbol{C}}_{dd} + \boldsymbol{C}_d)^{-1}(\boldsymbol{d}_j - \widehat{\boldsymbol{d}}_j) \tag{16}$$

For $j = 1,2,[\ldots],N_e$ with N_e denoting the number of ensemble members and thus the ensemble size. Each ensemble member consists of a stochastically sampled model parameter realization and an associated model forecast. So N_e model realizations are required for the number of ensembles N_a. $\widehat{\boldsymbol{d}}_j = \mathscr{G}(\boldsymbol{m}_j)$ denotes forecasted values by the thermal model at the observation points. $\boldsymbol{d}_j = \boldsymbol{d}_{obs} + \epsilon_j$, where $\epsilon_j = \sqrt{\boldsymbol{C}_d}\boldsymbol{z}_j$, and $\boldsymbol{z}_j \approx \mathscr{N}(0, \boldsymbol{I}_{Nd})$. Therefore, $\boldsymbol{z}_j$ are n uncorrelated samples of the normal distribution. The $\sqrt{\boldsymbol{C}_d}$ can be found from eigenvalues and eigenvalue analysis. Alternatively, ϵ_j can be determined by using standard sequential Gaussian simulation methodologies adopting covariance matrix $\boldsymbol{C}_d$. The model parameter perturbations in the ensemble are determined in a similar way. So $\boldsymbol{m}_j = \boldsymbol{m} + \epsilon_j$, where $\epsilon_j = \sqrt{\boldsymbol{C}_m}\boldsymbol{z}_j$. $\widehat{\boldsymbol{C}}_{md}$ and $\widehat{\boldsymbol{C}}_{dd}$ are determined from the ensemble runs:

$$\widehat{\boldsymbol{C}}_{md} = \frac{1}{N_e - 1}\ \boldsymbol{M}'\boldsymbol{D}'^{T} \tag{17}$$

Table 7
Overview of the number of sampled 20 by 20 km grid cells from the temperature data compilation from Limberger et al. (2014) (Fig. 5) and corresponding uncertaintiy range per depth level.

Depth (km)	Number of cells	Uncertainty range [± °C]		
		0 wells	1–5 wells per cell	> 5 wells per cell
1	17,035	7	5	3
2	24,970	9	7	5
3	2301	11	9	7
4	2023	13	11	9
5	1581	15	13	11
6	108	17	15	13

$$\hat{C}_{dd} = \frac{1}{N_e - 1} \quad \boldsymbol{D'D'}^T \tag{18}$$

which are covariance matrix estimates, with $\boldsymbol{M} = \{\boldsymbol{m}_0, \boldsymbol{m}_1, [...], \boldsymbol{m}_{N_e}\}$, $\boldsymbol{D} = \{\mathcal{G}(\boldsymbol{m}_0), \mathcal{G}(\boldsymbol{m}_1), [...], \mathcal{G}(\boldsymbol{m}_{N_e})\}$, and primes denote column vectors consisting of anomalies with respect to the mean value of that particular column.

The ensemble smoother of Eq. (16) provides a direct solution if a linear relationship exists between model parameters and forecast. If that is not the case, such as for radiogenic heat production and thermal conductivity, the ensemble smoother requires multiple iterations.

Emerick and Reynolds (2013) introduced a procedure to improve data matches obtained with an Ensemble Smoother (ES) for non-linear problems based on assimilating the same data multiple times with an inflated covariance matrix of the measurement errors ($\boldsymbol{C_d}$). This procedure – denoted as ES-MDA – can be interpreted as an iterative ES, where the number of iterations N_a has to be chosen *a priori*. The ES-MDA method can be summarized as follows:

1. Define the number of iterations of the data assimilation N_a and the multiplication coefficients of the data covariance matrix $\boldsymbol{\alpha}_i$ for $i = 1,2,[\ldots],N_a$;
2. Initialize the ensemble model parameters $\boldsymbol{m}_j$, using sequential Gaussian simulation based on model prior estimate $\boldsymbol{m}$ and parameter covariance matrix $\boldsymbol{C}_m$;
3. For $i = 1$ to N_a:
   (a) Perturb the ensemble of observations, replacing $\boldsymbol{C_d}$ with $\boldsymbol{\alpha}_i \boldsymbol{C_d} \rightarrow \epsilon_j = \sqrt{\alpha_i}\sqrt{C_d}\boldsymbol{z}_j$
   (b) Update the ensemble $\boldsymbol{m}_j$ using Eq. (13) with the scaled $\boldsymbol{\alpha}_i C_d$.

For our model, we used a sequential data assimilation approach where the mean results of the final ensemble of the first data assimilation sequence was used as input for the following sequence. Compared to a data assimilation approach where all model parameters are varied simultaneously, the sequential approach has more degrees of freedom for the parameter variation which results in a better fit with the observations.

3.4. Model uncertainty

The stochastic prior thermal parameters of the model are drawn from a double triangular or uniform distribution, in which the P50 value corresponds to the deterministic value of the properties, as a function of lithology, temperature and pressure. Different probability distributions were chosen for specific layers in the models (Table 6). These probability distributions were marked by a spatial correlation, determined through a variogram. For each data assimilation sequence, different variogram ranges were chosen based on the expected spatial variability. These variogram ranges determined the area of influence of each perturbation. We assumed the temperature variation at the lower boundary condition of the model to be relatively smooth compared to the expected variation of thermal conductivity in the top 5 km.

For our first data assimilation sequence, the temperature of the lower boundary condition of the model was varied stochastically with a constant value between T-400, T+400. Temperature uncertainty was represented by a triangular distribution.

Radiogenic heat production in the upper crust was varied for our second data assimilation sequence. The uncertainty of radiogenic heat production was represented by a triangular distribution with a scaling factor from 0.1 to 3 times the original prior value of A. The variogram range was set to a radius of 300 km.

For our final data assimilation sequence, bulk thermal conductivity was varied stochastically in the top 15 km of our model (Table 6). The uncertainty was represented by a uniform distribution with a depth-dependent scaling factor ranging from 0.5 to 1.5 times the prior value at the surface, to 0.75 to 1.25 times the prior value at 15 km depth. We assumed that bulk thermal conductivities at the surface would have the largest variation, as uncertainties of the original depositional porosity determine the mixing ratio between conductive rock matrix and poorly conductive pore fluids (Eq. (4)). At greater depth, the porosity is more or less constant and differences between bulk thermal conductivities become less pronounced. To allow smaller-scale spatial variation we set the variogram range to a radius of 100 km.

3.5. Data uncertainty

As observations for our model calibration, we sampled temperature maps compiled by Limberger et al. (2014) (Fig. 5) at regular distances for depth intervals of 1 km up to a depth of 6 km. The sampling resulted in 35533 data points in total, each point representing a 20 by 20 km grid cell. Data uncertainty was represented by a Gaussian distribution, with a depth-dependent standard deviation that corresponds to the amount of boreholes inside each grid cell of the temperature maps (Table 7). Borehole locations were obtained from the geothermal atlas (Hurter and Haenel, 2002) and from The Global Heat Flow Database of the International Heat Flow Commission (2018).

4. Prior and posterior model

The results of the forward thermal model and subsequent data assimilation yielded two new thermal models of the European subsurface. Temperature data derived from wells were only incorporated into the posterior model. In the following sections, we discuss the prior and posterior model results including: temperature, temperature misfits, and thermal properties. For the posterior model, we used the mean results of the final ensemble of the data assimilation sequence where the thermal conductivity was varied. The main results of the thermal modeling are presented in the form of modeled temperature and misfit maps (Figs. 7 to 13), misfit graphs (Fig. 14), and 1D vertical profiles and cross sections (Figs. 15 to 20). Additional maps of the prior and posterior thermal properties can be found in the Appendix A. For selected locations, the main results of the model are visualized in vertical 1D profiles, where prior and posterior temperatures and thermal properties are plotted (Figs. 15 and 20) as well as the misfit evolution throughout the data assimilation sequences (Fig. 16).

To gain insight on the cause of temperature misfits, we present misfit maps from 1 to 5 km depth (Figs. 7 to 11) and misfit profiles for selected locations (Fig. 16). We assign negative misfits if the model underestimated the temperature compared to the observations and positive misfits if the model overestimated the temperature. Areas that are expected to be significantly affected by non-conductive heat transfer, such as regions with active tectonics or volcanism, show large temperature misfits. It is important to note that the data assimilation

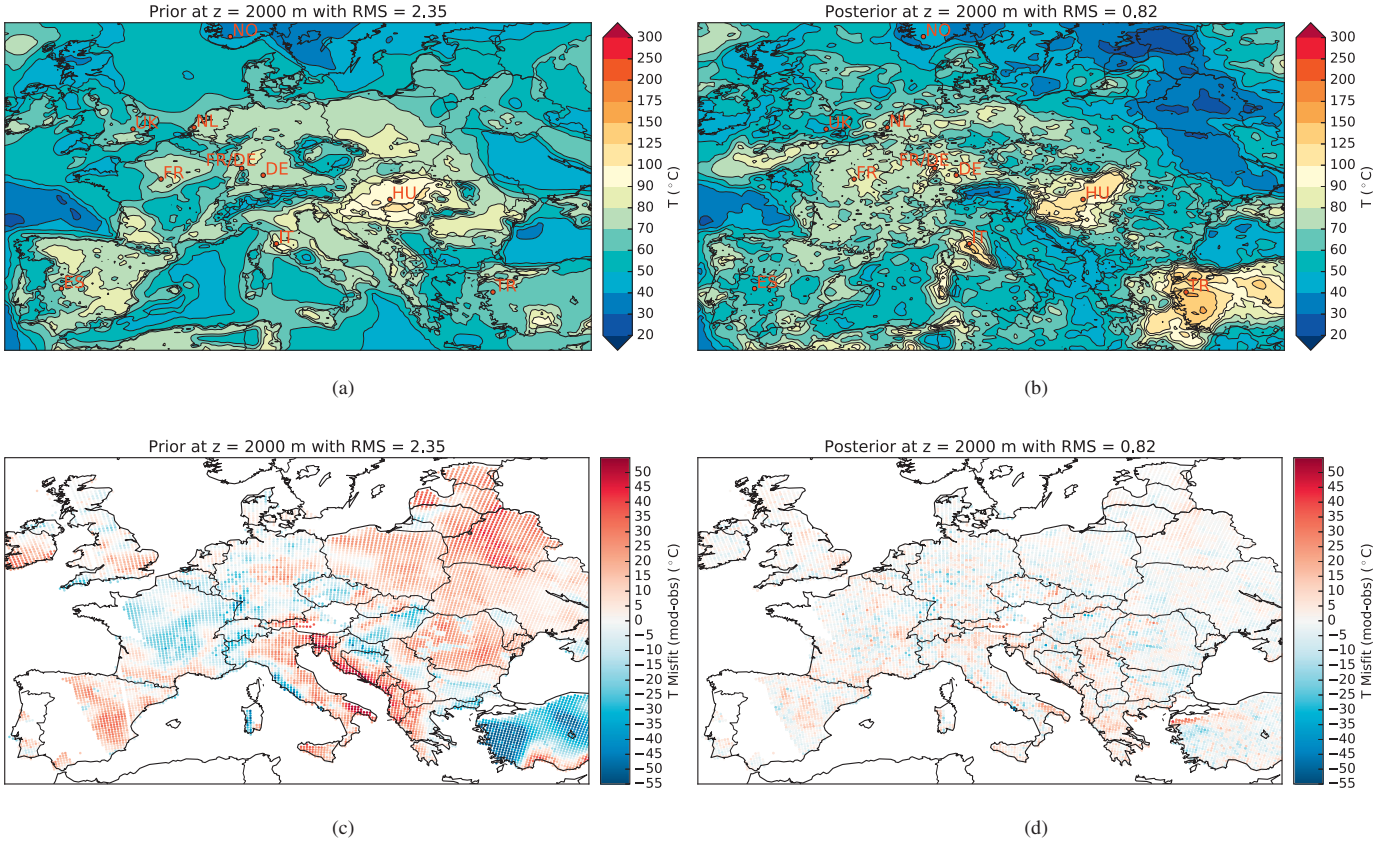

Fig. 8. (a) Temperatures of the prior 3D temperature model at 2000 m depth. (b) Temperatures of the posterior 3D temperature model at 2000 m depth. (c) Misfit of prior model. (d) Misfit of posterior model.

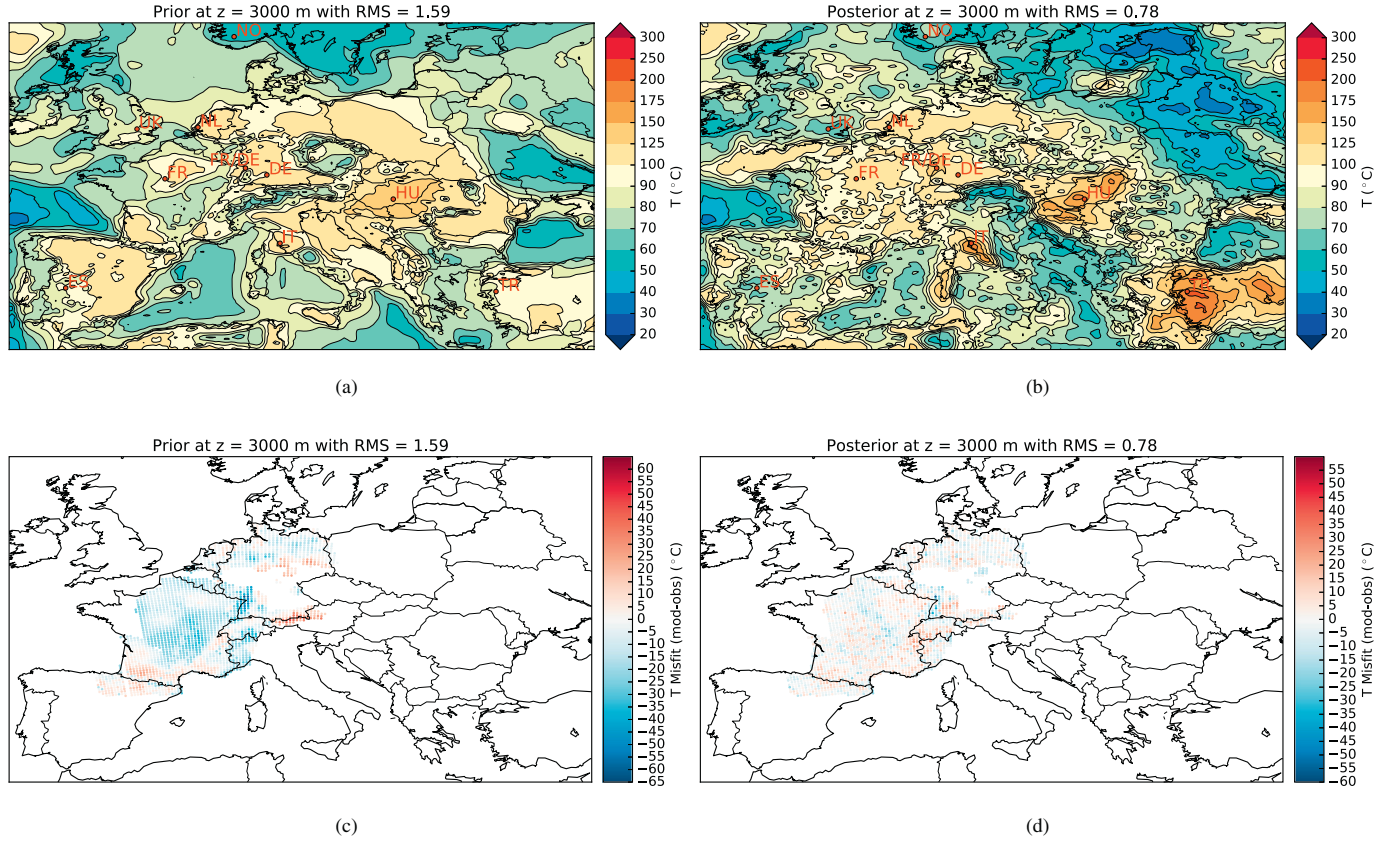

Fig. 9. (a) Temperatures of the prior 3D temperature model at 3000 m depth. (b) Temperatures of the posterior 3D temperature model at 3000 m depth. (c) Misfit of prior model. (d) Misfit of posterior model.

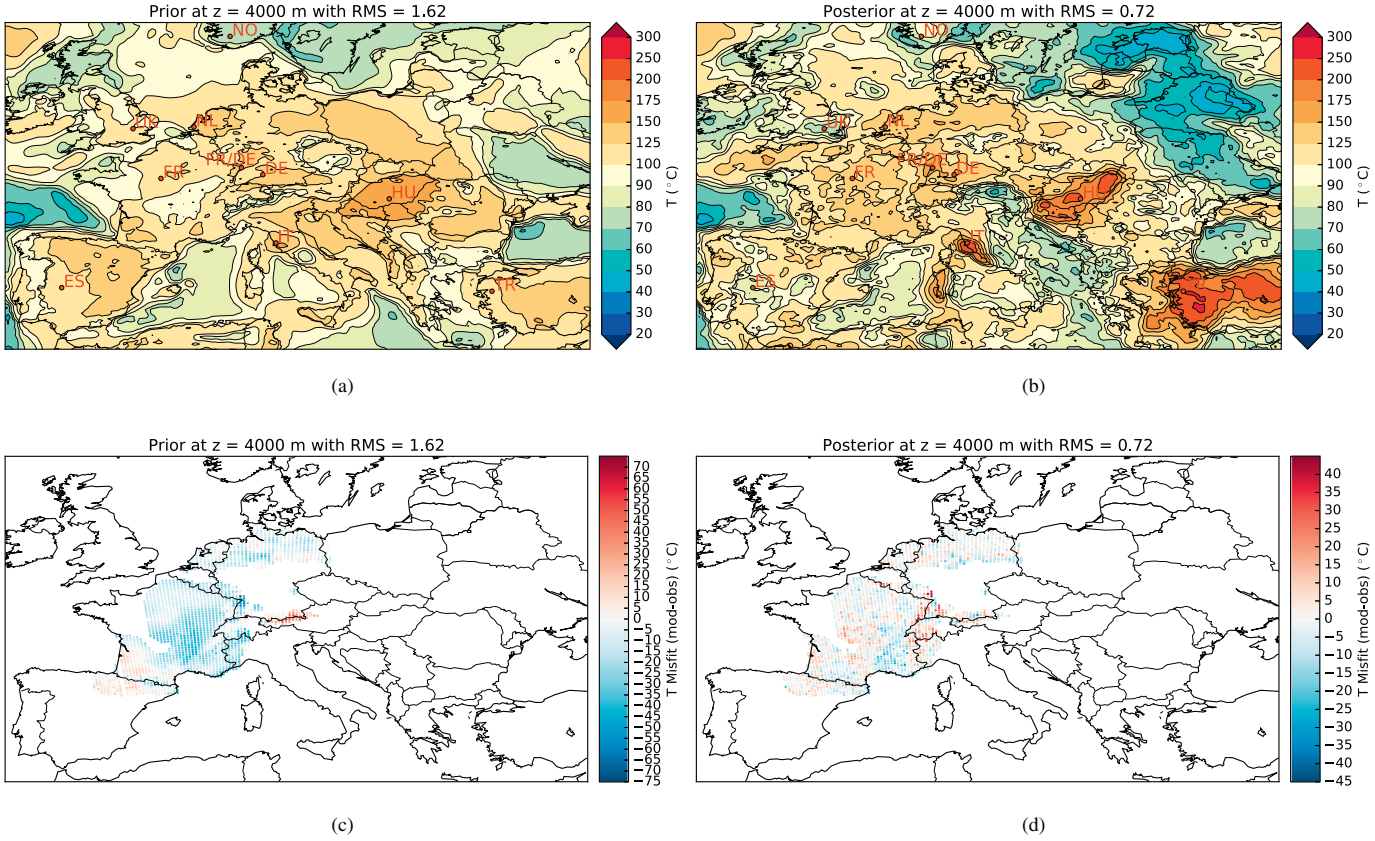

Fig. 10. (a) Temperatures of the prior 3D temperature model at 4000 m depth. (b) Temperatures of the posterior 3D temperature model at 4000 m depth. (c) Misfit of prior model. (d) Misfit of posterior model.

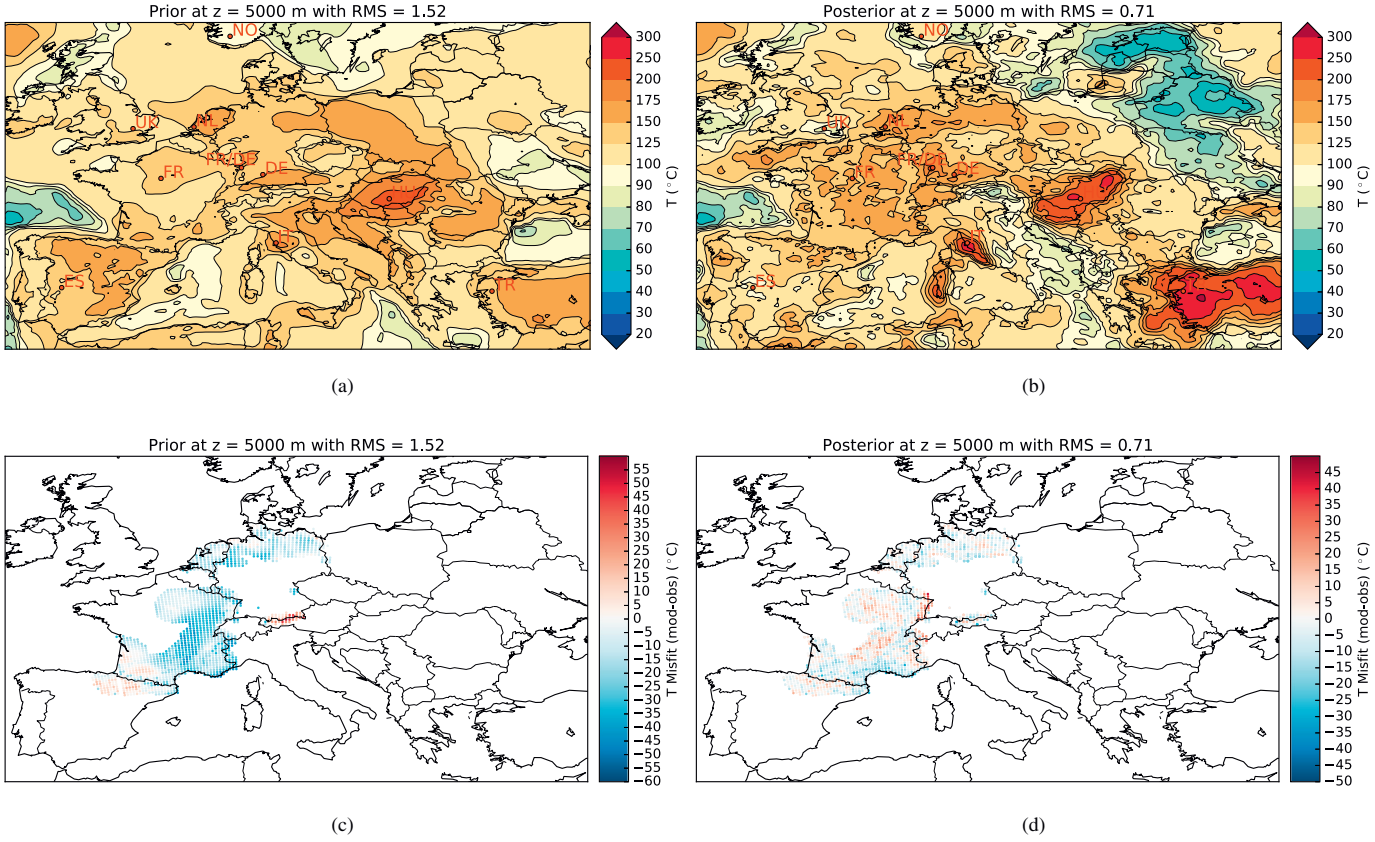

Fig. 11. (a) Temperatures of the prior 3D temperature model at 5000 m depth. (b) Temperatures of the posterior 3D temperature model at 5000 m depth. (c) Misfit of prior model. (d) Misfit of posterior model.

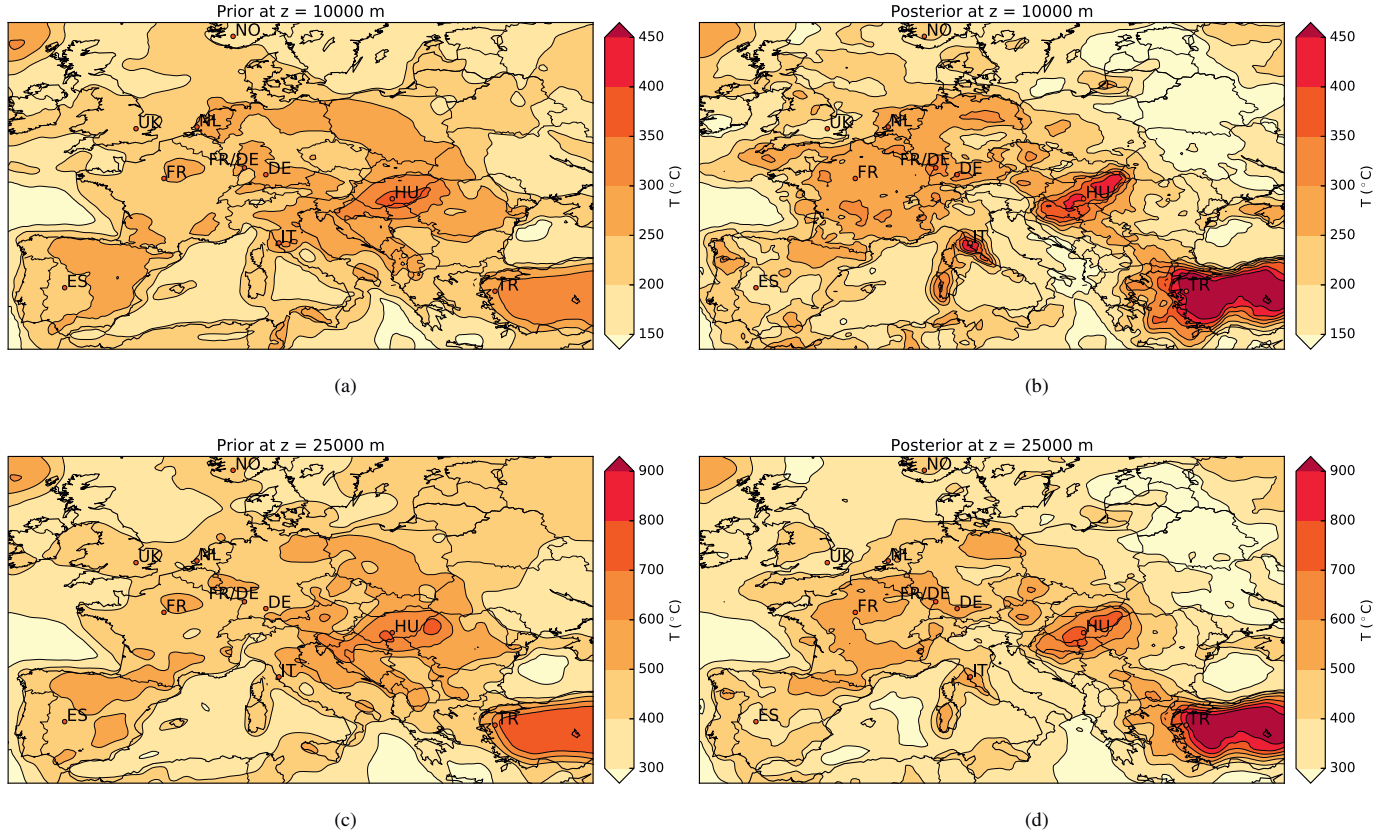

Fig. 12. (a) Temperatures of the prior 3D temperature model at 10 km depth. (b) Temperatures of the posterior 3D temperature model at 10 km depth. (c) Temperatures of the prior 3D temperature model at 25 km depth. (d) Temperatures of the posterior 3D temperature model at 25 km depth.

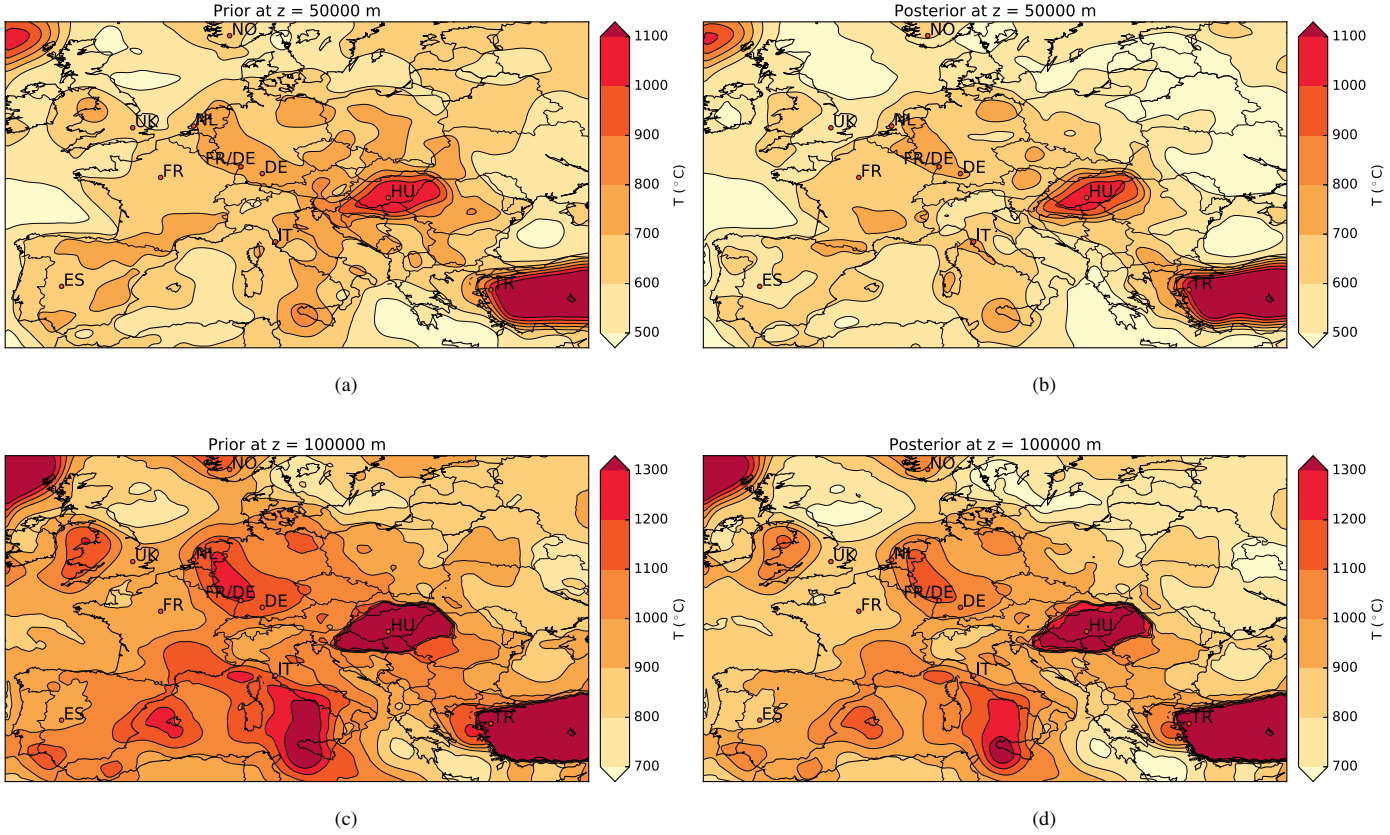

Fig. 13. (a) Temperatures of the prior 3D temperature model at 50 km depth. (b) Temperatures of the posterior 3D temperature model at 50 km depth. (c) Temperatures of the prior 3D temperature model at 100 km depth. (d) Temperatures of the posterior 3D temperature model at 100 km depth.

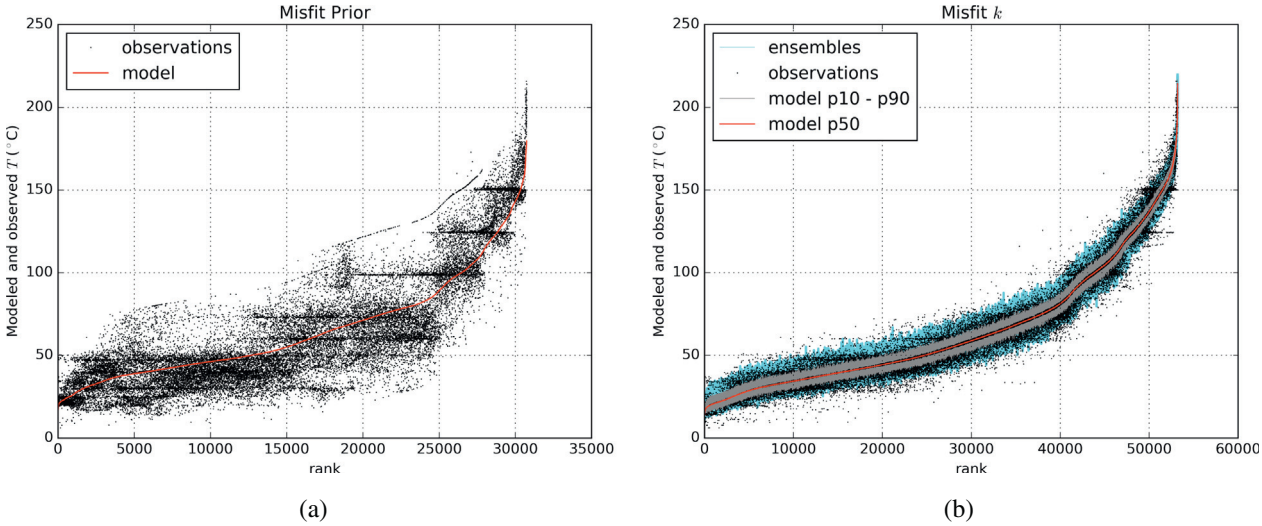

Fig. 14. Distributions of temperature ranked by the modeled temperatures at each observation point for the prior model (a) and the final data assimilation sequence where the thermal conductivity is varied. In both graphs, black dots are the observations points. In (a), the thick red curve is a line through the modeled values and the black dots are the observed values. In (b), the thick red curve is a line through the P50 values of the modeled temperatures, black dots are the observed values, the gray lines are the P10 and P90 values of the modeled temperatures, and the thick blue lines are the modeled temperatures for all the 300 ensemble members of the final ensemble. If the observations are near the model line there is a good fit. Comparing (a) and (b), clearly shows how the model fit improves after applying our sequential ES-MDA work flow. (For interpretation of the references to color in this figure legend, the reader is referred to the web version of this article.)

routine incorporates a part or all of these non-conductive heat transfer effects by changing the model parameters within the predefined distribution range (Table 6). Inevitably, assumptions on *a priori* thermal properties are also partly causing these misfits, as well as the simplification and generalization of our model into a four-layered system.

Due to the lack of a detailed structural model with faults, we did not consider the effects of shear heating in major faults and shear zones. Several studies show that shear heating can lead to a significant local temperature raise up to several hundreds of degrees locally (Brun and Cobbold, 1980; Molnar and England, 1990; Leloup et al., 1999; Burg and Gerya, 2005; Souche et al., 2013). The amount of heat generated over time is controlled by the size, strain rates, and the total duration of movement along shear zones and fault plains. In some long-lasting shear zones, such as large thrusts near subduction zones, the heat generation can be considered as a pseudo steady-state thermal effect (Molnar and England, 1990; Burg and Gerya, 2005).

To analyze the fit of the prior model and the effectiveness of the data assimilation, we show the distributions of temperature ranked by the modeled temperatures at each observation point for the prior model (Fig. 14a), and for the final data assimilation sequence where the thermal conductivity was varied (Fig. 14b). Comparing the prior and posterior model shows an improved fit after applying our sequential ES-MDA work flow: most observation points plot much closer to the P50 results of the posterior model. However, the variation within the data points remains larger than the bandwidth of the variation of the computed ensembles, indicating that our ES-MDA approach was not entirely capable of producing the required variation that would lead to a further reduction of the misfits. An increase in bandwidth of the ensembles could be achieved by allowing more variation within the model parameters or by imposing a very shallow heat flow boundary condition.

4.1. Thermal structure

A comparison between modeled prior and posterior temperatures at 2 km depth (Fig. 8a and b), where most observations are available, shows a significant different distribution. Both models share the same large-scale thermal features, such as the clear NW-SE striking Trans-European Suture Zone. It separates the young and dynamic Phanerozoic Europe in the SW from the old and cratonic Precambrian Europe in the NE (e.g. Balling, 1995; Pharaoh, 1999; Smit et al., 2016). Inside the Phanerozoic domain, the posterior model is characterized by higher temperatures, apart from the Eastern Alps and Dinarides. At 2-5 km depth (Figs. 8 to 11), important geothermal regions such as the European Cenozoic Rift System (ECRIS) (FR/DE), Pannonian Basin (HU), Tuscany (Lardarello) (IT), Paris Basin (FR) and western Anatolia (TR) show on the posterior model map as clear thermal anomalies.

As expected, the largest negative temperature misfits at 1 km and 2 km of the prior model are found in these geothermal regions and can be attributed to extensional tectonics for the ECRIS (Dèzes et al., 2004) and Pannonian Basin (Horváth et al., 2015) and - in combination with volcanic activity - in Tuscany (Bellani et al., 2004). High radiogenic heat production in rocks from crystalline basement and thermal blanketing of low conductive shale-rich sediments is thought to be the cause of the Paris basin thermal anomaly (Bonté et al., 2010). The Central European Basin System (Basin system ranging from eastern United Kingdom to western Poland, see Fig. 1a and b) is also marked by elevated temperatures, mainly caused by the thick layer of siliciclastic sediments with a low thermal conductivity (e.g. van Wees et al., 2000; Bonté et al., 2012; Scheck-Wenderoth et al., 2014).

The largest positive misfits of the prior model are located around the Adriatic Sea, in the northern part of Sicily, in southern Ireland, and in parts of the Eastern European Craton (EEC). The Dinarides and large parts of Italy are covered by thick carbonate sediments. Large-scale fluid flow in these rocks that are associated with karstification could be the cause of these relatively low observed temperatures (Fernàndez et al., 1990; Ravnik et al., 1995; Kooi, 2016).

In the German part of the Molasse Basin east of Munich, a negative thermal anomaly can be observed in both the prior and posterior models (Fig. 8b). This region shows a large positive temperature misfit in our prior model. This can partially be explained by the deepening of the LAB towards the Alps and the presence of the granitic Tauern Window Body, imposing a large thermal conductivity contrast with the juxtaposed sediments (Przybycin et al., 2015). However, as shown by Przybycin et al. (2017), the observed negative thermal anomaly can

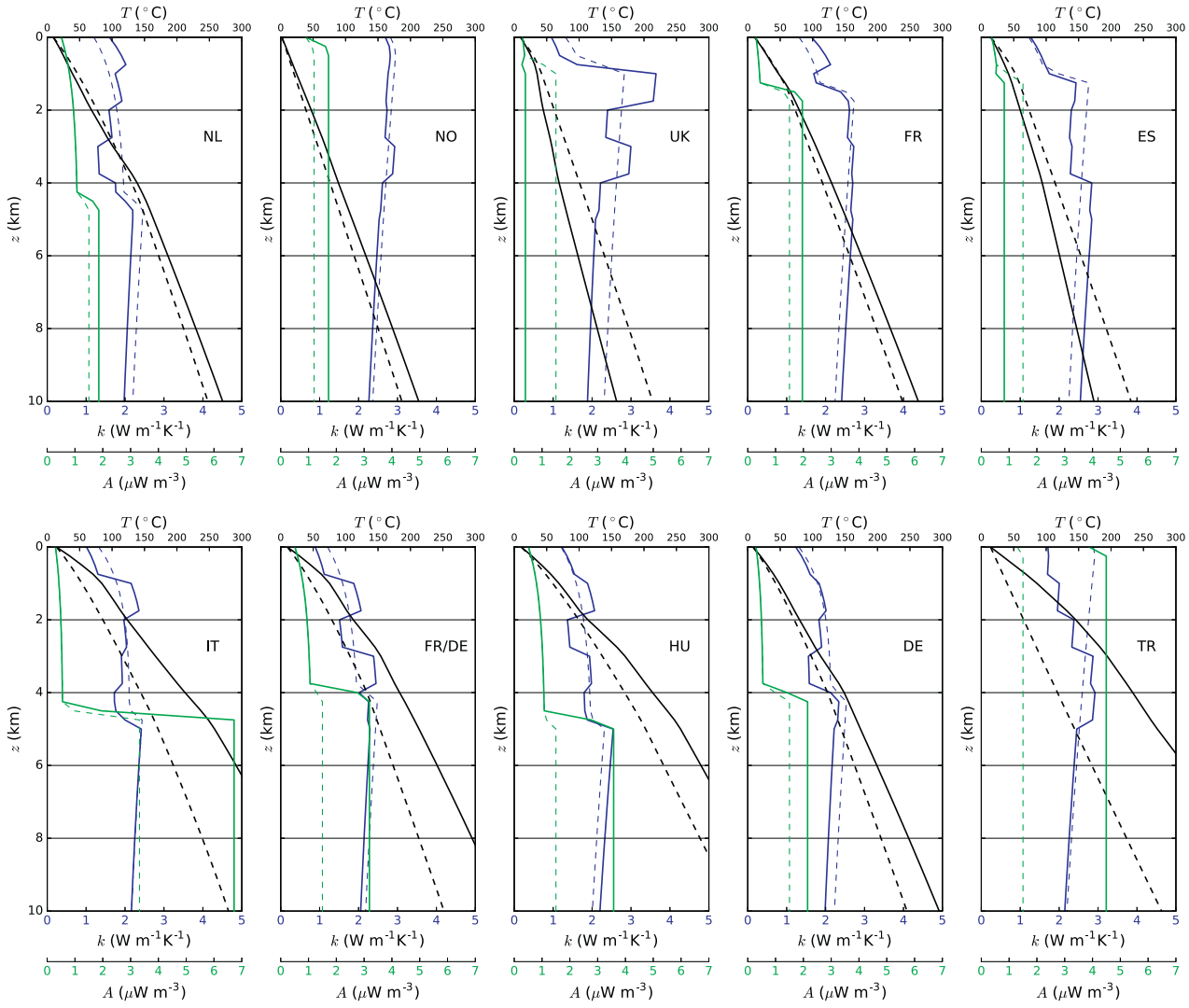

(a)

Fig. 15. 1D profiles up to 10 km depth extracted from the model showing prior (dashed lines) posterior (normal lines) thermal properties and boundary conditions: Geothermal gradients in black, radiogenic heat production in green, and (bulk) thermal conductivity in blue. Country codes in the profiles correspond to the country codes of the maps. (For interpretation of the references to color in this figure legend, the reader is referred to the web version of this article.)

only fully be reproduced by taking into account effects of basin-wide groundwater flow. In the posterior model this misfit is largely reduced.

The large positive misfit in the prior model in the southern part of Ireland could be caused by an underestimation of the initial radiogenic heat production (Noller et al., 2015). The low prior thermal conductivity values assigned to the East European Platform sediments within the East European Craton (EEC) cause an overestimation of temperatures. These meta-sediments are up to 650 Myr old and have experienced several phases of deformation including extension, inversion and compression (Nikishin et al., 1996), leading to metamorphism and a likely associated increase of bulk thermal conductivity.

While posterior misfits at 1 to 5 km depth are much smaller and are within range of the errors for the observations (RMS < 1), the lack of temperature data at greater depths makes it difficult to asses the accuracy in the deeper parts of our model.

The deep thermal structure (Figs. 12, 13 and 17 to 19) shows a more erratic pattern in the 10 km and 25 km depth slices extracted from the posterior model. At these depths, changes in temperature of the posterior model are mostly limited to tectonically and/or volcanically active zones such as Upper Rhine Graben, Pannonian Basin, Tuscany and western Anatolia. By contrast, temperatures in the EEC are lower in the posterior model. At greater depths of 50 km and 100 km, the wavelength of the variability increases, partly due to more homogenous thermal conductivities and heat generation values chosen for the model. At 50 km depth, temperatures associated with the thermal LAB (~1200 °C) are already inferred below western Anatolia, the Pannonian Basin and northwest of the United Kingdom. The shallow LAB northwest of the United Kingdom marks the onset of the Atlantic ridge (Artemieva and Thybo, 2008).

4.2. Prior and posterior thermal properties

The prior total radiogenic heat generation in the upper crust (Fig. A.1a) is mostly controlled by the thickness of the upper crust while the volumetric heating rate is controlled by the lithology we assigned to the crust. For most onshore regions, the prior values vary between 1

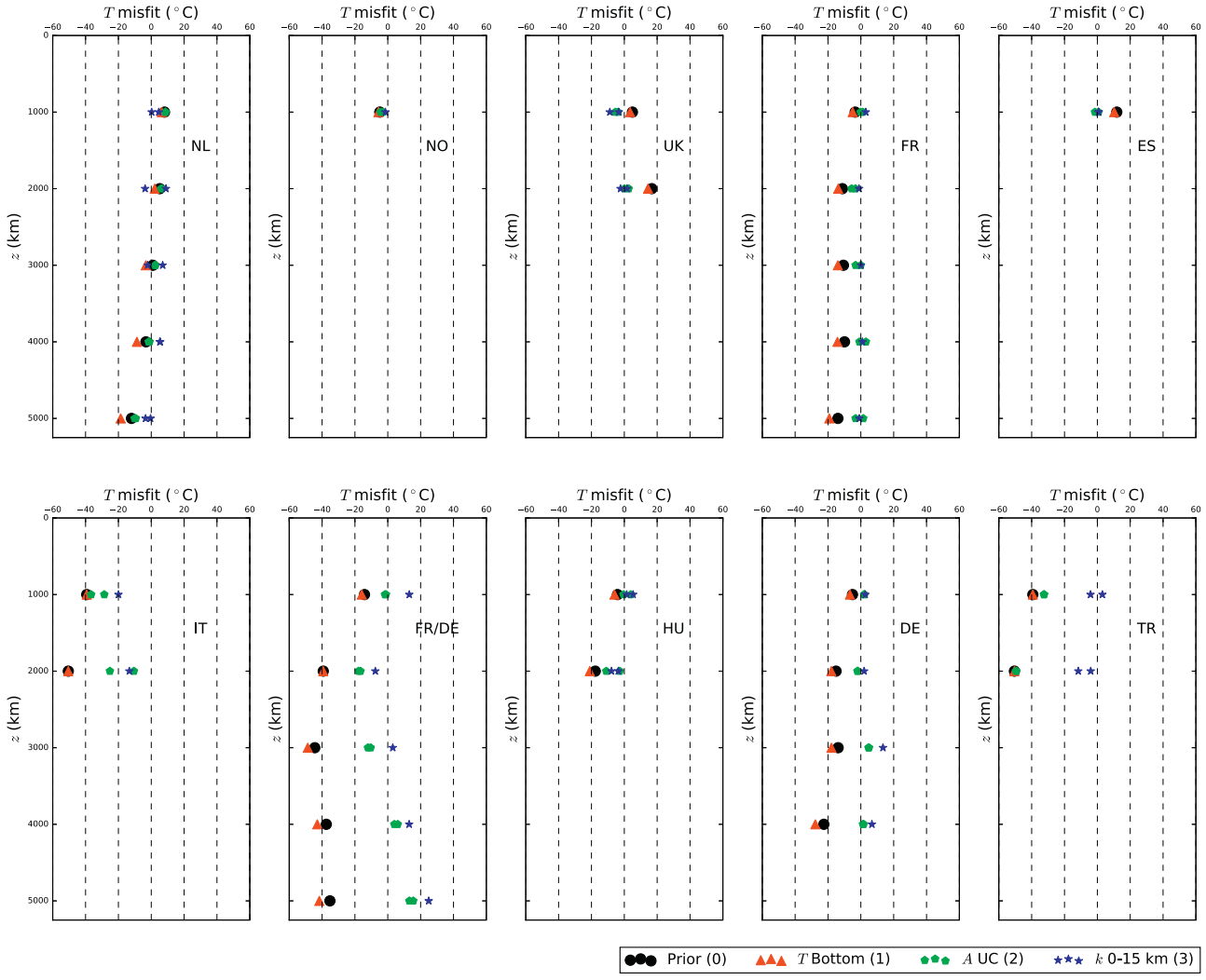

(a)

Fig. 16. 1D profiles of temperature misfit evolution throughout the data assimilation sequences: misfit of the prior model in black circles, misfit after varying the lower boundary condition in red triangles, radiogenic heat production in green pentagons, and (bulk) thermal conductivity in blue stars. Country codes in the profiles correspond to the country codes of the maps. (For interpretation of the references to color in this figure legend, the reader is referred to the web version of this article.)

and 2 μW m^{-3}. For oceanic crust or basaltic lithotypes (Figs. 2b and 3b) values are lower, as listed in Table 5.

The results of the ES-MDA do not change the large scale pattern of the upper crustal radiogenic heat generation distribution of the posterior model (Fig. A.1b), but an increase in heat production can be observed in areas with a large prior misfit. Lithosphere thinning in the European Cenozoic Rift System (Dèzes et al., 2004) and in the Pannonian Basin (Horváth et al., 2015) results in a shallower LAB in our model, also reflected in the observations as high temperatures. Within the constraints of the model parametrization, our method minimized misfits with these high observed temperatures by increasing the posterior radiogenic heat generation to 3-5 μW m^{-3} in the upper crust (HU in Figs. 15 and 20), whereas these high observed temperatures are more likely caused by transient effects of lithosphere thinning in the Pannonian basin (Békési et al., 2018).

Back-arc extension and subsequent crustal thinning by delamination (Bartol and Govers, 2014), Eocene to Miocene magmatic intrusions (Altunkaynak et al., 2012), and transport of hot fluids through fault zones (Bilim et al., 2016) could explain the high inferred posterior radiogenic heat generation in the upper crust of Turkey (TR in Figs. 15 and 20). Below the Massif Central, crustal thinning caused by a possible mantle plume (e.g. Lucazeau et al., 1984; Sobolev et al., 1997) could explain the high inferred posterior heat generation simulating the shallow transient effect of increased heat flow. However, there are little reliable data on the deep thermal structure beneath the Massif Central. Also the three-dimensional shape of this possible mantle plume is poorly constrained. In our approach, we mainly vary thermal properties in the shallow part of the model to obtain a better model fit with the shallow thermal imprint that could be caused by this plume. This makes our deep temperatures in this region highly uncertain.

Even though Tuscany (IT in Figs. 15 and 20) already had a predefined heat generation of more than 3 μW m^{-3} (Table 5), it still required values up to 9 μW m^{-3} to simulate transient effects of heat flow related to lithosphere extension, mantle up-doming, and magma

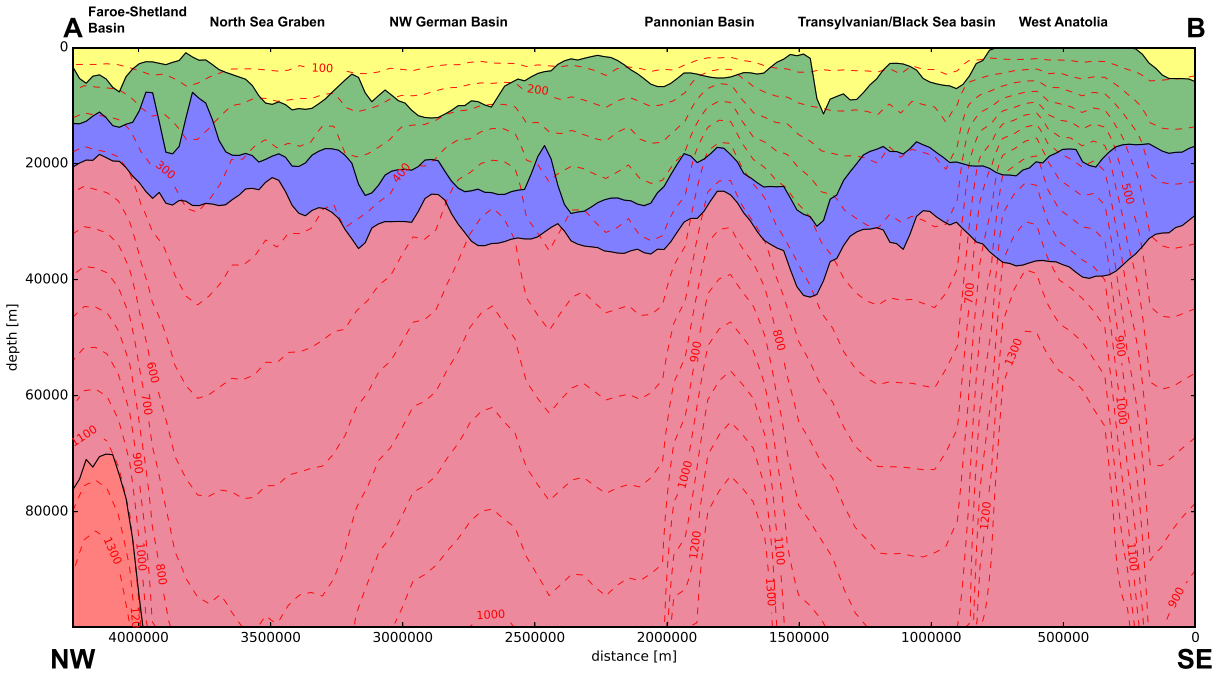

Fig. 17. 2D cross section from the Faroe-Shetland Basin to western Anatolia (AB in Fig. 1a) with posterior temperatures plotted over the structural model up to 100 km depth. Yellow, green, blue, pink, and red layers correspond to sediments, upper crust, lower crust, lithospheric mantle, and asthenosphere, respectively. Note that the initial thermal LAB from the structural model no longer corresponds to the 1200 °C isotherm of the posterior model. (For interpretation of the references to color in this figure legend, the reader is referred to the web version of this article.)

intrusions, as well as fault-controlled convection in sedimentary layers and crystalline basement (Cameli et al., 1993; Bellani et al., 2004; Della Vedova et al., 2008).

Prior in situ thermal conductivity at 2 km depth (Fig. A.4a in the Appendix A) follows the lithotypes inferred from the surface geology (Fig. 1b). It is characterized by high values > 2.75 $W m^{-1} K^{-1}$ where the crystalline basement is outcropping at the surface (Armorican shield, Anatolia, Baltic Shield, East European Platform). Low values < 2 $W m^{-1} K^{-1}$ were assigned to deep basins containing unconsolidated sediments, such as the Southern Permian basin or Central

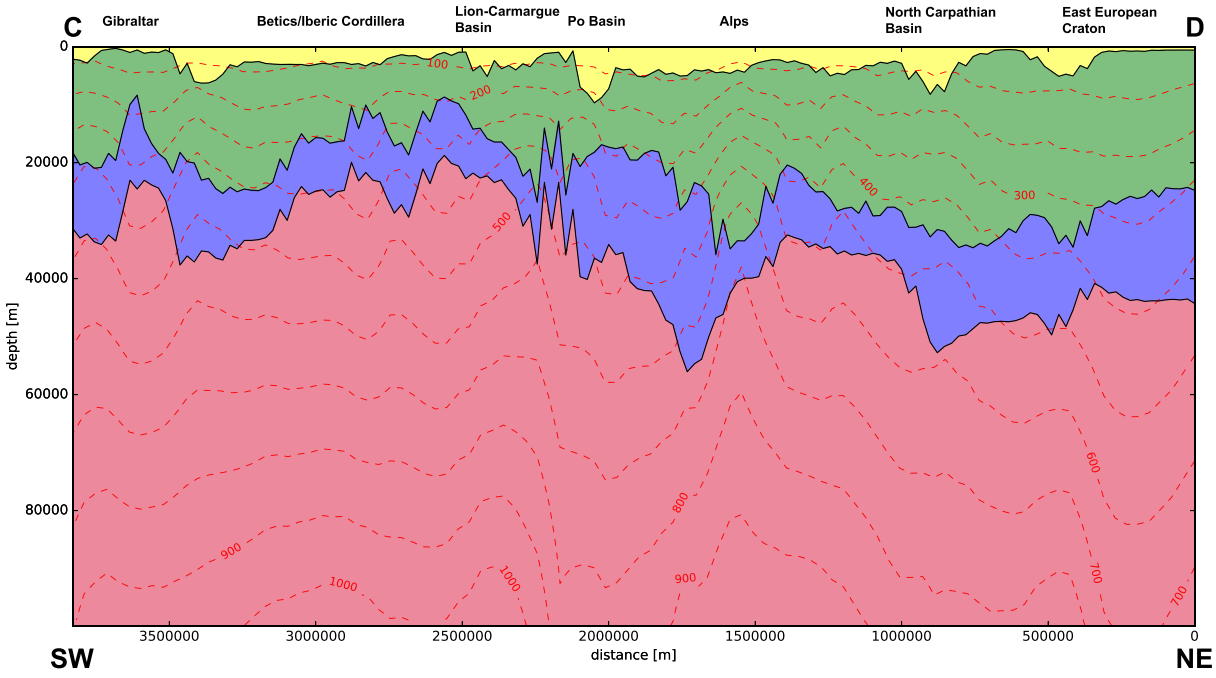

Fig. 18. 2D cross section from Gibraltar to the East European Craton (CD in Fig. 1a) with posterior temperatures plotted over the structural model up to 100 km depth. Yellow, green, blue, pink, and red layers correspond to sediments, upper crust, lower crust, lithospheric mantle, and asthenosphere, respectively. Note that the initial thermal LAB from the structural model no longer corresponds to the 1200 °C isotherm of the posterior model. (For interpretation of the references to color in this figure legend, the reader is referred to the web version of this article.)

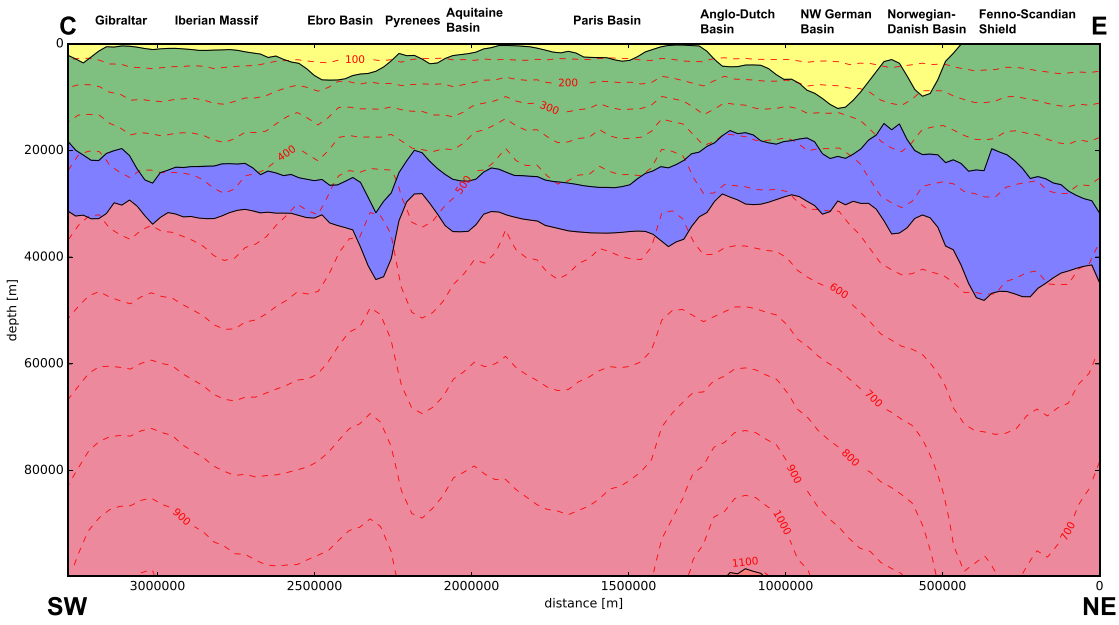

Fig. 19. 2D cross section from Gibraltar to the Fenno-Scandian SHield (CE in Fig. 1a) with posterior temperatures plotted over the structural model up to 100 km depth. Yellow, green, blue, pink, and red layers correspond to sediments, upper crust, lower crust, lithospheric mantle, and asthenosphere, respectively. Note that the initial thermal LAB from the structural model no longer corresponds to the 1200 °C isotherm of the posterior model. (For interpretation of the references to color in this figure legend, the reader is referred to the web version of this article.)

European Basin System, Pannonian Basin, Po Basin and Transylvanian Basin (Fig. 1b). Apart from showing a more noisy pattern, the regional trends of the prior thermal conductivity distribution are still visible in the posterior model. Significant increases of the thermal conductivity in the posterior model were inferred in regions within cratonic areas such as EEC and Fennoscandia, but also in parts of the United Kingdom (most notably in Scotland), Greece, Bulgaria, Turkey, France (most notably the Massif Central area), and in the Alps (Tauern Window). Sediment age and effects of uplift and erosion of deeply buried sediments were not incorporated in the prior model, likely causing the required increase in posterior thermal conductivity to minimize misfits with the observed low temperatures.

Lower values of posterior thermal conductivity are inferred in the Norwegian-Danish basins, the Pannonian Basin, along the coast of western Anatolia, and in large parts of the Balkans. In the Norwegian-Danish basins, in particular the Glükstadt Graben, lower posterior thermal conductivity values were required to fit higher observed temperatures associated with heat chimney effects of deeper lying highly conductive salt structures (Scheck-Wenderoth and Maystrenko, 2013; Balling et al., 2013; Fuchs and Balling, 2016). The Pannonian Basin and the coast of western Anatolia required a combination of a stronger thermal blanketing effect with an already strongly increased upper crustal heat production, to fully compensate for the underestimated prior temperatures due to non-conductive and transient effects (HU and TR in Figs. 15 and 20).

5. Discussion and conclusion

To bridge the gap between large-scale geophysical models and more detailed basin-scale models, we constructed a 3D thermal model of the European lithosphere with differentiated thermal properties for specific domains within each crustal layer. To improve model robustness, the lower boundary condition, radiogenic heat production, and thermal conductivity were stochastically varied and calibrated using an ES-MDA technique to obtain a good fit with available temperature data. Lacking a European centralized and public database of temperature measurements, our model was calibrated with 35533 temperature points extracted from regional temperature models. Northeast of the TESZ, the calibrated model predicts geothermal gradients to lie mainly below 20 °C km^{-1} up to 10 km depth. Southwest of the TESZ, the model predicts gradients ranging from 20 °C km^{-1} near the Adriatic coast to more than 50 °C km^{-1} in volcanically active regions.

This study provides physics-based reference models and underlying properties, compositional reference models, boundary conditions and observational data constraints at EU scale for thermal characterization. Evidently, this approach at EU scale, is – in principle – not different from simulating active processes at regional scale to site scale. Local model refinement is generally targeted at improving robustness by including more detail in modeled heat transfer processes as well as better constraints in model properties and boundary conditions.

A large number of misfits of our prior thermal model with the temperature observations can be attributed to transient thermal effect or to areas where a significant amounts of non-conductive heat transfer is occurring such as regions with active tectonics or magmatism. Other misfits in our model are likely related to both the generalization required for building a European-scale model and to *a priori* assumptions on thermal properties and model boundary conditions. The former can be used to study the contribution of non-conductive heat transfer to surface heat flow, while the latter can be used to study lithosphere thermal properties. We minimized both misfits by applying the ES-MDA technique. However, our *a posteriori* values of thermal properties cannot simply be used as input for other models. Especially in large parts of the European continent affected by transient thermal effects or large-scale non-conductive heat transfer, where our *a posteriori* thermal properties were significantly changed to fit the modeled temperatures to the observations within a steady-state heat transfer approach. Therefore, our *a posteriori* values of thermal properties need to be treated with care as they may mimic transient or non-conductive effects not included in the

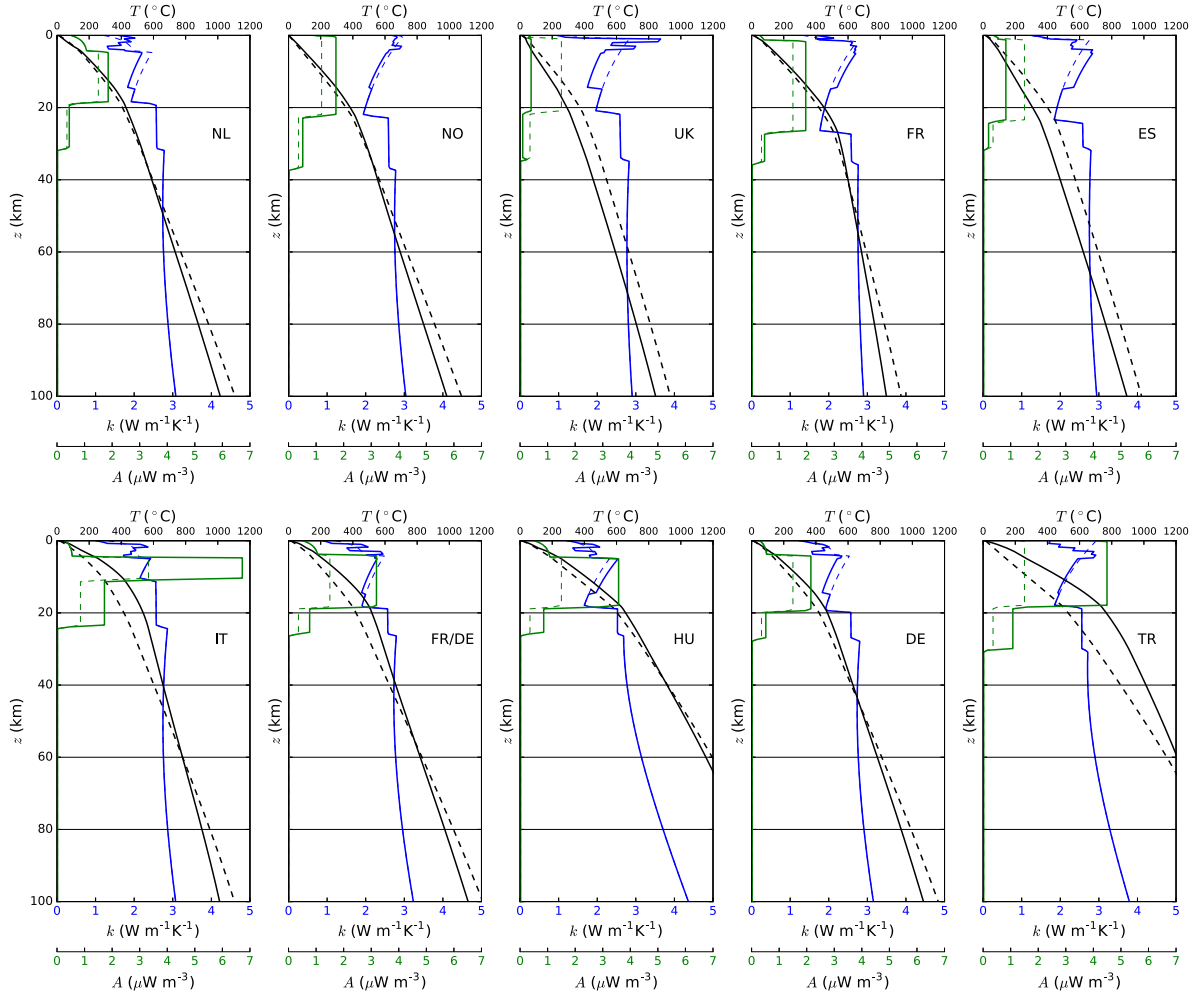

Fig. 20. 1D profiles up to 100 km depth extracted from the model showing prior (dashed lines) posterior (normal lines) thermal properties and boundary conditions: Geothermal gradients in black, radiogenic heat production in green, and (bulk) thermal conductivity in blue. Country codes in the profiles correspond to the country codes of the maps. (For interpretation of the references to color in this figure legend, the reader is referred to the web version of this article.)

model, rather than true property values. On the other hand, extreme corrections in the posterior properties clearly signal the existence of non-conductive and transient processes in the Earth's crust. The identification of non-conductive effects could considerably assist in assessment of the robustness of the model for extrapolation of observed shallow thermal gradients to deeper depth levels. The latter is subject to large uncertainty in case of non-conductive effects.

At regional scale, conduction controls the thermal field in large parts of Europe. In particular in regions such as Fennoscandia and the Eastern European Craton where the lithosphere is old and stable and in thermal steady-state. In many regions southwest of the Trans-European Suture Zone, conduction alone is not sufficient to explain the observed temperatures because the conductive thermal field is likely disturbed by active tectonic processes and volcanism. Buoyancy-driven thermal convection and advective groundwater flow can also significantly affect geothermal gradients when sufficient permeability is present.

We imposed conduction as the only way to transfer heat through our model, making it difficult to quantify contributions of other heat transfer mechanisms to the surface heat flow. We varied the main conductive parameters, Z_{LAB}, A, and k, to obtain a good overall fit with the data points. However, the variation within the data points remains larger than the bandwidth of the variation of the computed ensembles, indicating that our ES-MDA approach was not entirely capable of producing the required variation for all regions and conditions. We allowed variation of these parameters within bounds of what would be physically reasonable. However, a number of regions required such a significant change to their *a priori* conductive parameters, even to non-realistic values, that other processes and/or other heat transfer mechanisms are likely to have disturbed their conductive thermal fields.

Acknowledgments

The research leading to these results has received funding from the EC Seventh Framework Programme under grant agreement no. 608553 (Project IMAGE).

Appendix A

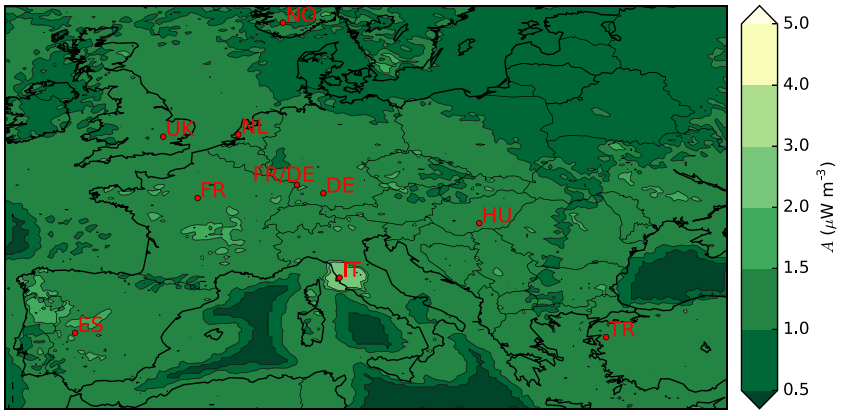

(a)

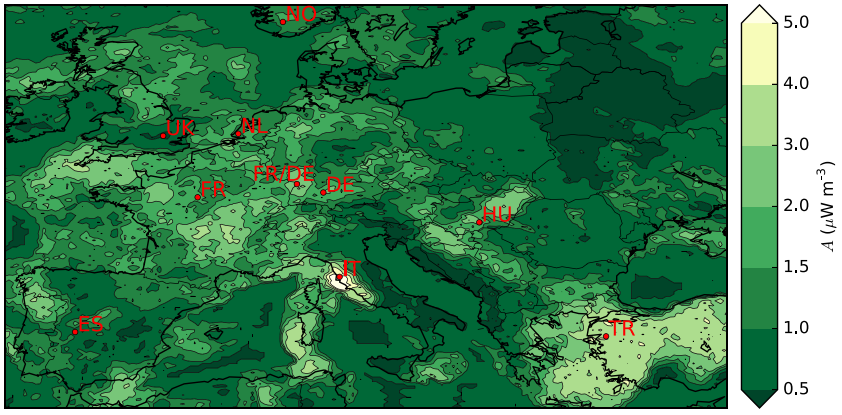

(b)

Fig. A.1. (a) Map of the radiogenic heat generation in the upper crust of the prior model conform Table 5. (b) Map of the radiogenic heat generation in the upper crust of the posterior model. NO = Norway, UK = United Kingdom, NL = West Netherlands basin in the Netherlands, FR = Paris Basin in France, FR/DE = Upper Rhine Graben part of the European Cenozoic Rift System (ECRIS), DE = Molasse Basin in Germany, HU = Pannonian Basin in Hungary, IT = Lardarello geothermal region in Tuscany, Italy, TR = Western Anatolia in Turkey, ES = Spanish Central System.

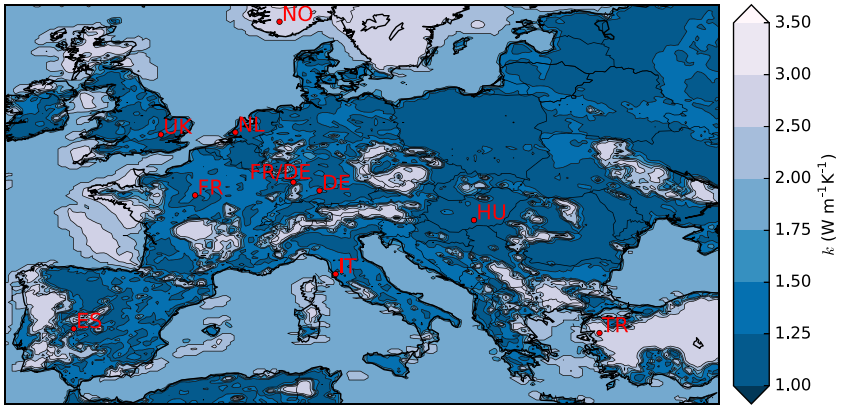

(a)

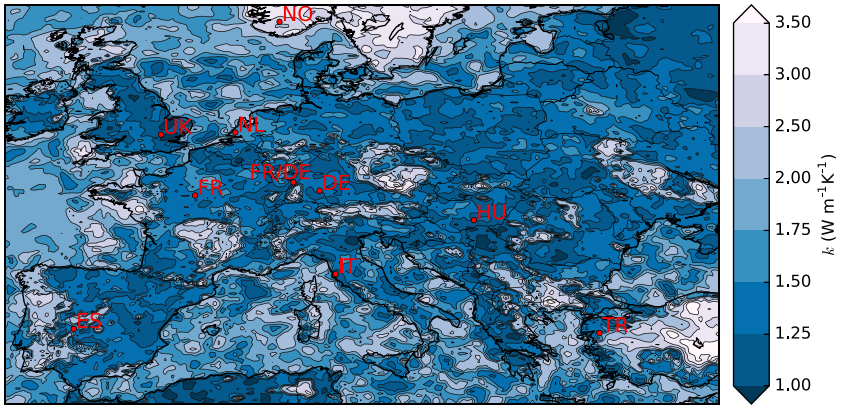

(b)

Fig. A.2. (a) Map of the (bulk) thermal conductivity at the surface of the prior model conform the surface lithology in Fig. 1a and Tables 1 to 3 and 5. (b) Map of the surface (bulk) thermal conductivity of the posterior model.

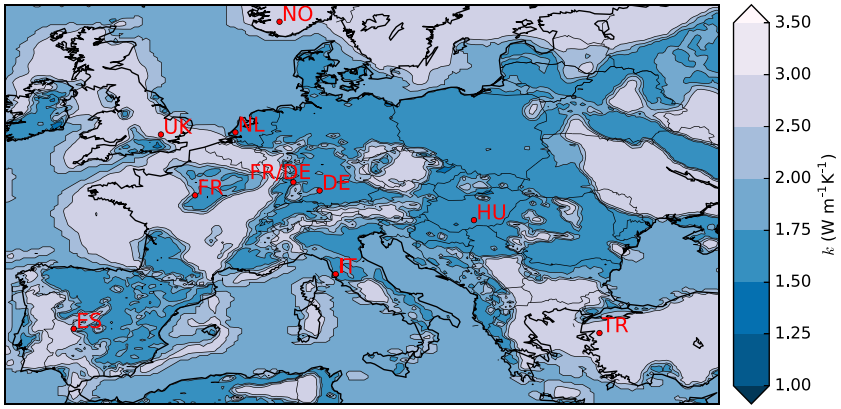

(a)

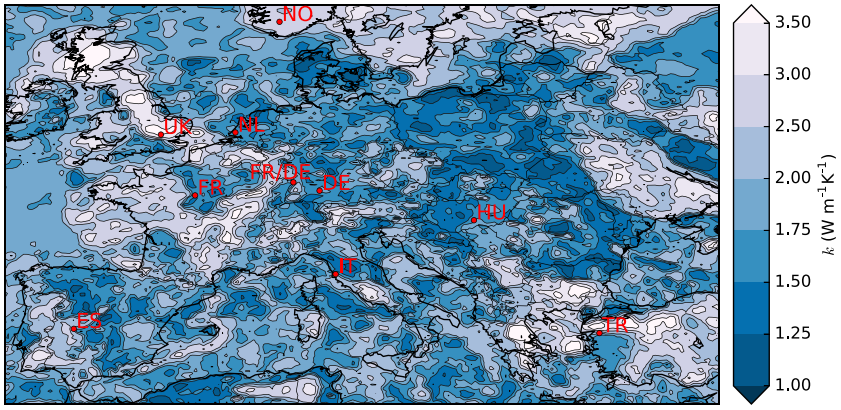

(b)

Fig. A.3. (a) Map of the (bulk) thermal conductivity at 1 km depth of the prior model conform the surface lithology in Fig. 1a and Tables 1 to 3 and 5. (b) Map of the (bulk) thermal conductivity at 1 km depth of the posterior model.

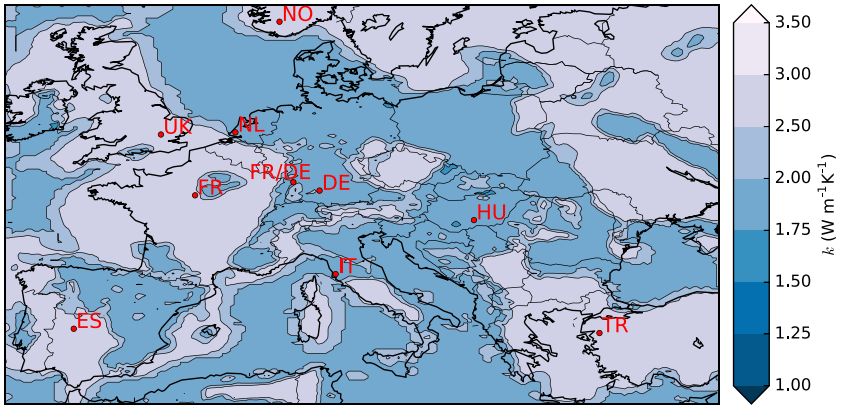

(a)

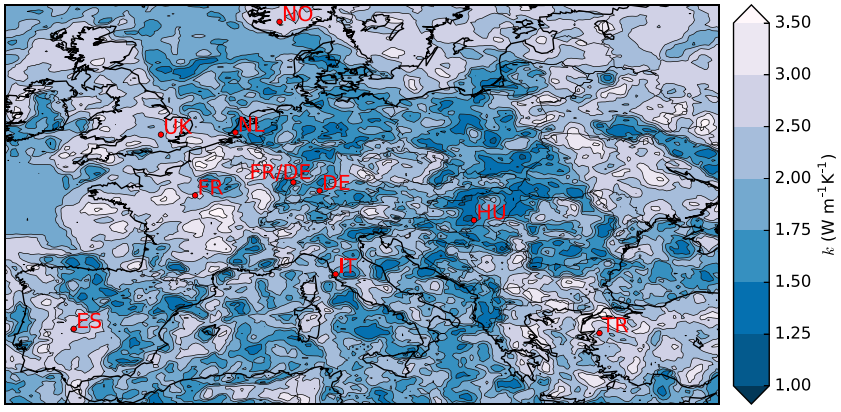

(b)

Fig. A.4. (a) Map of the (bulk) thermal conductivity at 2 km depth of the prior model conform the surface lithology in Fig. 1a and Tables 1 to 3 and 5. (b) Map of the (bulk) thermal conductivity at 2 km depth of the posterior model.

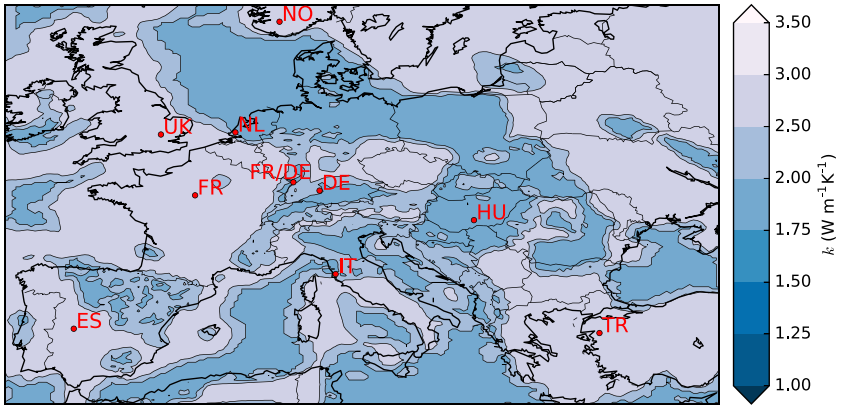

(a)

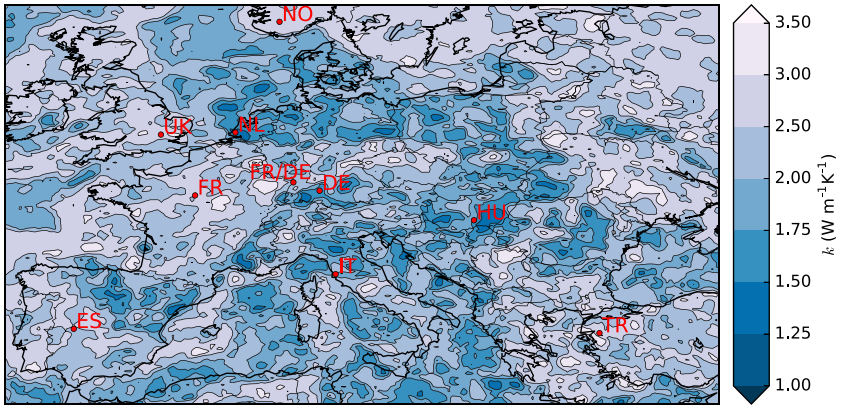

(b)

Fig. A.5. (a) Map of the (bulk) thermal conductivity at 3 km depth of the prior model conform the surface lithology in Fig. 1a and Tables 1 to 3 and 5. (b) Map of the (bulk) thermal conductivity at 3 km depth of the posterior model.

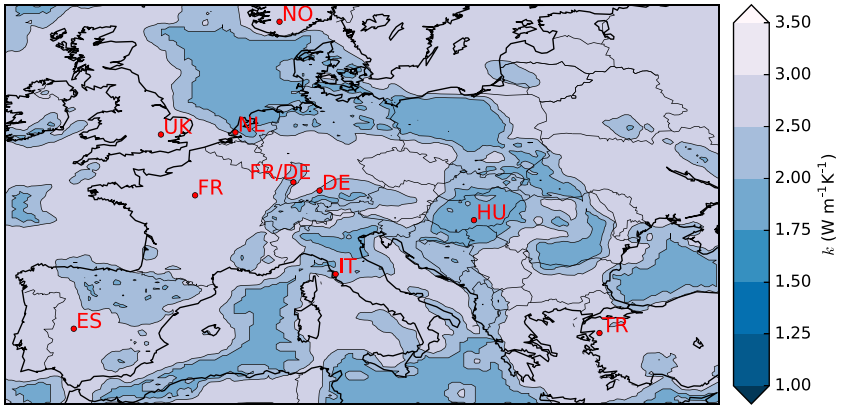

(a)

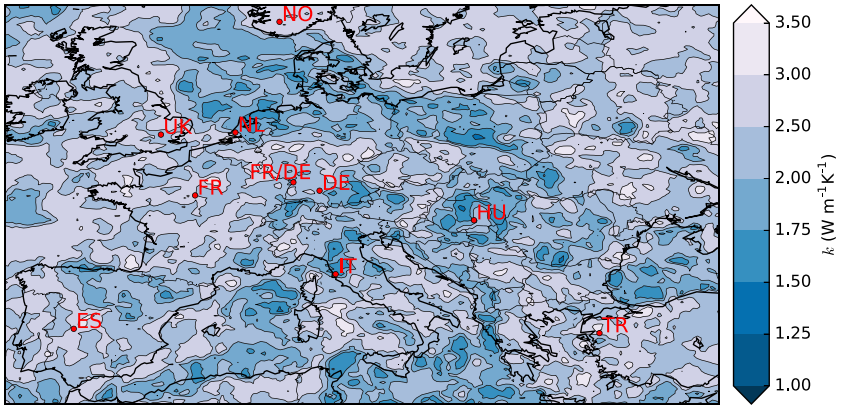

(b)

Fig. A.6. (a) Map of the (bulk) thermal conductivity at 4 km depth of the prior model conform the surface lithology in Fig. 1a and Tables 1 to 3 and 5. (b) Map of the (bulk) thermal conductivity at 4 km depth of the posterior model.

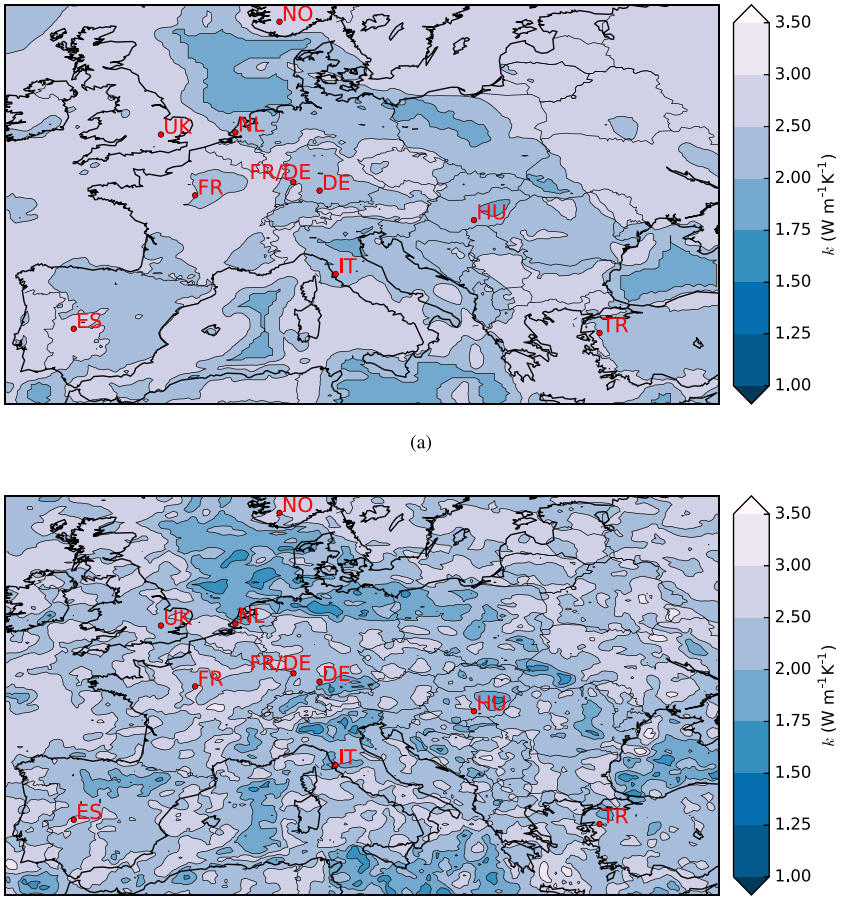

(a)

(b)

Fig. A.7. (a) Map of the (bulk) thermal conductivity at 5 km depth of the prior model conform the surface lithology in Fig. 1a and Tables 1 to 3 and 5. (b) Map of the (bulk) thermal conductivity at 5 km depth of the posterior model.

References

Altunkaynak, Ş., Dilek, Y., Genç, C., Sunal, G., Gertisser, R., Furnes, H., Foland, K., Yang, J., 2012. Spatial, temporal and geochemical evolution of Oligo-Miocene granitoid magmatism in western Anatolia, Turkey. Gondwana Res. 21, 961–986.

Amante, C., Eakins, B., 2009. ETOPO1 1 Arc-Minute Global Relief Model: Procedures, Data Sources and Analysis. In: NOAA Technical Memorandum NESDIS NGDC-24, . http://www.ngdc.noaa.gov/mgg/global/relief/ETOPO1/docs/ETOPO1.pdf.

Angus, D., Wilson, D., Sandvol, E., Ni, J., 2006. Lithospheric structure of the Arabian and Eurasian collision zone in eastern Turkey from S-wave receiver functions. Geophys. J. Int. 166, 1335–1346.

Artemieva, I., 2013. What is the lithosphere? In: The lithosphere: an interdisciplinary approach. Cambridge University Press, United Kingdom, pp. 1–14 Ch. 1, ISBN 978-0-521-84396-6.

Artemieva, I., Thybo, H., 2008. Deep Norden: highlights of the lithospheric structure of Northern Europe, Iceland, and Greenland. Episodes 31, 98–106.

Artemieva, I., Thybo, H., Kaban, M., 2006. Deep Europe today: geophysical synthesis of the upper mantle structure and lithospheric processes over 3.5 Ga. Geol. Soc. Lond. Spec. Publ. 32, 11–41.

Ascolese, E., Aurisicchio, A., Briggs-Smith, M., Mita, D., Perna, G., Rossi, S., Gaeta, F., 1993. Thermodynamics of water-permeated unwelded pyroclasts, 2: non-equilibrium properties. J. Volcanol. Geotherm. Res. 57, 235–251.

Athy, L., 1930. Density, porosity and compaction of sedimentary. AAPG Bull. 14, 1–24.

Balling, N., 1995. Heat flow and thermal structure of the lithosphere across the Baltic Shield and northern Tornquist Zone. Tectonophysics 244, 13–50.

Balling, P., Maystrenko, Y., Scheck-Wenderoth, M., 2013. The deep thermal field of the Glueckstadt Graben. Environ. Earth Sci. 70, 3505–3522.

Bär, K., Strom, A., Reinsch, T., Sippel, J., Freymark, J., Mielke, P., Wiesner, P., 2016. IMAGE petrophysical catalogue – an international database for reservoir characterization. In: Proceedings European Geothermal Congress 2016. European Geothermal Energy Council, Strasbourg, France.

Bartol, J., Govers, R., 2014. A single cause for uplift of the Central and Eastern Anatolian plateau. Tectonophysics 637, 116–136.

Beardsmore, G., Cull, J., 2001. Crustal Heat Flow: A Guide to Measurement and Modelling. Cambridge University Press, Cambridge, UJ0-521-79289-4.

Békési, E., Lenkey, L., Limberger, J., Porkoláb, K., Balázs, A., Bonté, D., Vrijlandt, M., Horváth, F., Cloetingh, S., van Wees, J.-D., 2018. Lithospheric-scale subsurface temperature model of the Hungarian part of the Pannonian Basin. Glob. Planet. Chang this volume.

Bellani, S., Brogi, A., Lazzarotto, A., Liotta, D., Ranalli, G., 2004. Heat flow, deep temperatures and extensional structures in the Larderello Geothermal Field (Italy): constraints on geothermal fluid flow. J. Volcanol. Geotherm. Res. 132, 15–29.

Bilim, F., Akay, T., Aydermir, A., Kosaroglu, S., 2016. Curie point depth, heat-flow and radiogenic heat production deduced from the spectral analysis of the aeromagnetic data for geothermal investigation on the Menderes Massif and the Aegean Region, western Turkey. Geothermics 60, 44–57.

Bonté, D., Guilloi-Frottier, L., Garibaldi, C., Bourgine, B., Lopez, S., Bouchot, V., Lucazeau, F., 2010. Subsurface temperature maps in French sedimentary basins: new data compilation and interpolation. Bull. Soc. Geol. Fr. 181, 377–390.

Bonté, D., Van Wees, J.-D., Verweij, J., 2012. Subsurface temperature of the onshore Netherlands: new temperature dataset and modelling. Geol Mijnb.-NJG 91, 491–515.

Brun, J., Cobbold, P., 1980. Strain heating and thermal softening in continental shear zones: a review. J. Struct. Geol. 2, 149–158.

Burg, J., Gerya, T., 2005. The role of viscous heating in Barrovian metamorphism of collisional orogens: thermomechanical models and application to the Lepontine Dome in the Central Alps. J. Metamorph. Geol. 23, 75–95.

Cameli, G., Dini, I., Liotta, D., 1993. Upper crustal structure of the Larderello geothermal field as a feature of post-collisional extensional tectonics (Southern Tuscany, Italy). Tectonophysics 224, 413–423.

Cermak, V., 1993. Lithospheric thermal regimes in Europe. Phys. Earth Planet. Inter. 79, 179–193.

Chapman, D., 1986. Thermal gradients in the continental crust. Geol. Soc. Lond. Spec. Publ. 24, 63–70.

Della Vedova, B., Vecellio, C., Bellani, S., Tinivella, U., 2008. Thermal modelling of the Larderello geothermal field (Tuscany, Italy). Int. J. Earth Sci. 97, 317–332.

Dèzes, P., Schmid, S., Ziegler, P., 2004. Evolution of the European Cenozoic Rift System: interaction of the Alpine and Pyrenean orogens with their foreland lithosphere. Tectonophysics 389, 1–33.

Dumas, P., van Wees, J.-D., Manzella, A., Nardini, I., Angelino, L., Latham, A., Simeoneva,

D., 2013. GEOELEC Report. In: Tech. rep. European Geothermal Energy Council (EGEC), Paris, France. http://www.geoelec.eu/.
Emerick, A., Reynolds, A., 2013. Ensemble smoother with multiple data assimilation. Comput. Geosci. 55, 3–15.
Evensen, G., 1994. Sequential data assimilation with a nonlinear quasi-geostrophic model using Monte Carlo methods to forecast error statistics. J. Geophys. Res. 99, 10143–10162.
Fernàndez, M., Torné, M., Zeyen, H., 1990. Modelling of thermal anomalies in the NW border of the Valencia through by groundwater convection. Geophys. Res. Lett. 17, 105–108.
Fuchs, S., Balling, N., 2016. Improving the temperature predictions of subsurface thermal models by using high-quality input data. Part 2: a case study from the Danish-German border region. Geothermics 64, 1–14.
Fullea, J., Muller, M., Jones, A., Afonso, J., 2014. The lithosphere-asthenosphere system beneath Ireland from integrated geophysical-petrological modeling II: 3D thermal and compositional structure. Lithos 189, 49–64.
Gaeta, F., De Natale, G., Peluso, F., Mastrolorenzo, G., Castagnolo, D., Troise, C., Pingue, F., Mita, D., Rossano, S., 1998. Genesis and evolution of unrest episodes at Campi Flegrei caldera: the role of thermal fluid-dynamical processes in the geothermal system. J. Geophys. Res. 103, 20921–20933.
Gaeta, F., Peluso, F., Arienzo, I., Castagnolo, D., De Natale, G., Milano, G., Albanese, C., Mita, D., 2003. A physical appraisal of a new aspect of bradyseism: the miniuplifts. J. Geophys. Res. 108, 2363.
Guo, W., Langevin, C., 2002. User's guide to SEAWAT: a computer program for simulation of three-dimensional variable-density ground-water flow. In: Tech. rep. U.S. Geological Survey, USA open-File Report 01-434.
Haenel, R. (Ed.), 1979. Atlas of subsurface temperatures in the European Community (EUR 6578 EN). The commission of the European Communities, Directorate-General Scientific and Technical Information and Information Management, Luxemburg.
Haenel, R., Staroste, E. (Eds.), 1988. Atlas of geothermal resources in the European Community, Austria and Switzerland (EUR 11026). Commission of the European Communities, Luxemburg ISBN 3-88746-221-1.
Hantschel, T., Kauerauf, A., 2009. Fundamentals of Basin and Petroleum Systems Modeling. Springer Berlin, Heidelberg, Germany978-3540723172.
Hartmann, J., Moosdorf, N., 2012. The new global lithological map database GLiM: a representation of rock properties at the Earth surface. Geochem. Geophys. Geosyst. 13, Q12004.
The Global Heat Flow Database of the International Heat Flow Commission, 2018. https://doi.org/10.17616/R3G305. Accessed 01 November 2016.
Hasterok, D., Chapman, D., 2011. Heat production and geotherms for the continental lithosphere. Earth Planet. Sci. Lett. 307, 59–70.
Hasterok, D., Webb, J., 2017. On the radiogenic heat production of igneous rocks. Geosci. Front. https://doi.org/10.1016/j.gsf.2017.03.006.
Hijmans, R., Cameron, S., Parra, J., Jones, P., Jarvis, A., 2005. Very high resolution interpolated climate surfaces for global land areas. Int. J. Climatol. 25, 1965–1978.
Hofmeister, A., 1999. Mantle values of thermal conductivity and the geotherm from phonon lifetimes. Science 283, 1699–1702.
Horváth, F., Musitz, B., Balász, A., Végh, A., Uhrin, A., Nádor, A., Koroknai, B., Pap, N., Tóth, T., Wórum, G., 2015. Evolution of the Pannonian basin and its geothermal resources. Geothermics 53, 328–352.
Hurter, S., Haenel, R. (Eds.), 2002. Atlas of Geothermal Resources in Europe (EUR 17811). Office for Official Publications of the European Communities, Luxemburg ISBN 92-828-0999-4.
Hurtig, E., Čermák, V., Haenel, R., Zui, V. (Eds.), 1992. Geothermal Atlas of Europe. Hermann Hack Verlagsgesellschaft: Geographisch-Kartographische Anstalt, Germany ISBN 3-7301-0034-3.
Jaupart, C., Labrosse, S., Mareschal, J.-C., 2007. Temperatures, heat and energy in the mantle of the Earth. In: Berdovici, D., Schubert, G. (Eds.), Treatise on Geophysics. vol. 7. Elsevier, Amsterdam, The Netherlands, pp. 253–303 Ch. Mantle Convection, ISBN 978-0-444-52748-6.
Jaupart, C., Mareschal, J.-C., Iarotsky, L., 2016. Radiogenic heat production in the continental crust. Lithos 262, 398–427.
Jokinen, J., 2000. Uncertainty Analysis and Inversion of Geothermal Conductive Models Using Random Simulation Methods. 7 Ph.D. thesis. University of Oulu, Oulu, Finland.
Jones, A., Afonso, J., Fullea, J., Salajegheh, F., 2014. The lithosphere-asthenosphere system beneath Ireland from integrated geophysical-petrological modeling - I: observations, 1D and 2D hypothesis testing and modeling. Lithos 189, 28–48.
Kind, R., Eken, T., Tilmann, F., Sodoudi, F., Taymaz, T., Bulut, F., Yuan, X., Can, B., Schneider, F., 2015. Thickness of the lithosphere beneath Turkey and surroundings from S-receiver functions. Solid Earth 6, 971–984.
Kooi, H., 2016. Groundwater flow as a cooling agent of the continental lithosphere. Nat. Geosci. 9, 227–230.
Koulakov, I., Kaban, M., Tesauro, M., Cloetingh, S., 2009. P and S velocity anomalies in the upper mantle beneath Europe from tomographic inversion of ISC data. Geophys. J. Int. 179, 345–366.
Lachenbruch, A., 1970. Crustal temperature and heat production: implications of the linear heat-flow relation. J. Geophys. Res. 75, 3291–3300.
Leloup, P., Ricard, Y., Battaglia, J., Lacassin, R., 1999. Shear heating in continental strike-slip shear zones: model and field examples. Geophys. J. Int. 136, 19–40.
Lenkey, L., Raáb, D., Goetzl, G., Lapanje, A., Nádor, A., Rajver, D., Rotár-Szalkai, A., Svasta, J., Zekiri, F., 2014. Lithospheric scale 3D thermal model of the Alpine-Pannonian transition zone. Acta Geod. Geophys. 52, 161–182.
Limberger, J., Bonté, D., de Vicente, G., Beekman, F., Cloetingh, S., van Wees, J.-D., 2017. A public domain model for 1D temperature and rheology construction in basement-sedimentary geothermal exploration: an application to the Spanish Central System and adjacent basins. Acta Geod. Geophys. 52, 269–282.
Limberger, J., Boxem, T., Pluymaekers, M., Bruhn, D., Manzella, A., Calcagno, P., Beekman, F., Cloetingh, S., van Wees, J.-D., 2018. Geothermal energy in deep aquifers: a global assessment of the resource base for direct heat utilization. Renew. Sustain. Energy Rev. 82, 961–975.
Limberger, J., Calcagno, P., Manzella, A., Trumpy, E., Boxem, T., Pluymaekers, M., van Wees, J.-D., 2014. Assessing the prospective resource base for enhanced geothermal systems in Europe. Geotherm. Energy Sci. 2, 55–71.
Lucazeau, F., Vasseur, G., Bayer, R., 1984. Interpretation of heat flow data in the French Massif Central. Tectonophysics 103, 99–119.
Molnar, P., England, P., 1990. Temperatures, heat flux, and frictional stress near major thrust faults. J. Geophys. Res. 95, 4833–4856.
Morgan, J., Chen, Y., 1993. The genesis of oceanic crust: magma injection, hydrothermal circulation, and crustal flow. J. Geophys. Res. 98, 6283–6297.
Morgan, J., Parmentier, E., Lin, J., 1987. Mechanisms for the origin of mid-ocean ridge axial topography: implications for the thermal and mechanical structure of accreting plate boundaries. J. Geophys. Res. 92, 12823–12846.
Nikishin, A., Ziegler, P., Stephenson, R., Cloetingh, S., Furne, A., Fokin, P., Ershov, A., Bolotov, S., Korotaev, M., Alekseev, A., Gorbachev, V., Shipilov, E., Lankreijer, A., Bembinova, E., Shalimov, I., 1996. Late Precambrian to Triassic history of the East European Craton: dynamics of sedimentary basin evolution. Tectonophysics 268, 23–63.
Noller, N., Daly, J., Team, The IRETHERM, 2015. The contribution of radiogenic heat production studies to hot dry rock geothermal resource exploration in Ireland. In: Proceedings of the World Geothermal Congress 2015. The International Geothermal Association, Melbourne, Australia.
Pharaoh, T., 1999. Palaeozoic terranes and their lithospheric boundaries within the Trans-European Suture Zone (TESZ): a review. Tectonophysics 314, 17–41.
Pollack, H., Hurter, S., Johnson, J., 1977. On the regional variation of heat flow, geotherms, and lithospheric thickness. Tectonophysics 38, 279–296.
Przybycin, A., Scheck-Wenderoth, M., Schneider, M., 2015. The 3D conductive thermal field of the North Alpine Foreland Basin: influence of the deep structure and the adjacent European Alps. Geotherm. Energy 3, 1–29.
Przybycin, A., Scheck-Wenderoth, M., Schneider, M., 2017. The origin of deep geothermal anomalies in the German Molasse Basin: results from 3D numerical models of coupled fluid flow and heat transport. Geotherm. Energy 5, 1–28.
Ravnik, D., Rajver, D., Poljak, M., živčić, M., 1995. Overview of the geothermal field of Slovenia in the area between the Alps, the Dinarides and the Pannonian basin. Tectonophysics 250, 135–149.
Rühaak, W., Bär, K., Sass, I., 2017. Estimating the subsurface temperature of Hessen/Germany based on a GOCAD 3D structural model - a comparison of numerical and geostatistical approaches. In: EGU General Assembly. European Geoscience Union, Vienna, Austria.
Schatz, J., Simmons, G., 1972. Thermal conductivity of Earth materials at high temperatures. J. Geophys. Res. 77, 6966–6983.
Scheck-Wenderoth, M., Cacace, M., Maystrenko, Y., Cherubini, Y., Noack, V., Kaiser, B., Sippel, J., Björn, L., 2014. Models of heat transport in the Central European Basin System: effective mechanisms at different scales. Mar. Pet. Geol. 55, 315–331.
Scheck-Wenderoth, M., Maystrenko, Y., 2013. Deep control on shallow heat in sedimentary basins. Energy Procedia 40, 266–275.
Schmelling, H., Marquart, G., 2014. A scaling law for approximating porous hydrothermal convection by an equivalent thermal conductivity: theory and application to the cooling oceanic lithosphere. Geophys. J. Int. 197, 645–664.
Schneider, F., Potdevin, J., Wolf, S., Faille, I., 1996. Mechanical and chemical compaction model for sedimentary basin simulators. Tectonophysics 263, 307–317.
Sekiguchi, K., 1984. A method for determining terrestrial heat flow in oil basinal areas. Tectonophysics 103, 67–79.
Smit, J., van Wees, J.-D., Cloetingh, S., 2016. The Thor suture zone: from subduction to intraplate basin setting. Geology 44, 707–710.
Smit, J., van Wees, J.-D., Cloetingh, S., 2018. Early Carboniferous extension in East Avalonia: 350 My record of lithospheric memory. Mar. Pet. Geol. 92, 1010–1027.
Sobolev, S., Granet, H.Z.M., Achauer, U., Bauer, C., Werling, F., Altherr, R., Fuchs, K., 1997. Upper mantle temperatures and lithosphere-asthenosphere system beneath the French Massif Central constrained by seismic, gravity, petrologic and thermal observations. Tectonophysics 275, 143–164.
Souche, A., Medvedev, S., Andersen, T., Dabrowski, M., 2013. Shear heating in extensional detachments: implications for the thermal history of the Devonian basins of W Norway. Tectonophysics 608, 1073–1085.
Tari, G., Dövényi, P., Dunkl, I., Horváth, F., Lenkey, L., Stefanescu, M., Szafián, P., Tóth, T., 1999. Lithospheric structure of the Pannonian basin derived from seismic, gravity and geothermal data. In: Durand, B., Horváth, F., Séranne, M. (Eds.), The Mediterranean Basins: Tertiary Extension within the Alpine Orogen. Geological Society, London, Special Publications, vol. 156. pp. 215–250.
Tašárová, A., Afonso, J., Bielik, M., Götze, H.-J., Hók, J., 2009. The lithospheric structure of the Western Carpathian—Pannonian Basin region based on the CELEBRATION 2000 seismic experiment and gravity modelling. Tectonophysics 475, 454–469.
Tesauro, M., Kaban, M., Cloetingh, S., 2008. EuCRUST-07: a new reference model for the European crust. Geophys. Res. Lett. 35, 1–5.
Tesauro, M., Kaban, M., Cloetingh, S., 2009. A new thermal and rheological model of the European lithosphere. Tectonophysics 476, 478–495.
van Wees, J.-D., Beekman, F., 2000. Lithosphere rheology during intraplate basin extension and inversion. Tectonophysics 320, 219–242.
van Wees, J.-D., Bergen, F., David, P., Nepveu, M., Beekman, F., Cloetingh, S., Bonté, D., 2009. Probabilistic tectonic heat flow modeling for basin maturation: assessment method and applications. Mar. Pet. Geol. 26, 536–551.
van Wees, J.-D., Stephenson, R., Ziegler, P., Bayer, U., McCann, T., Dadlez, R., Gaup, R.,

Narkiewicz, M., Bitzer, F., Scheck, M., 2000. On the origin of the Southern Permian Basin, Central Europe. Mar. Pet. Geol. 17, 43–59.
Vilà, M., Fernández, M., Jiménez-Munt, I., 2010. Radiogenic heat production variability of some common lithological groups and its significance to lithospheric thermal modeling. Tectonophysics 490, 152–164.
Xu, Y., Shankland, T., Linhardt, S., Rubie, D., Langenhorst, F., Klasinski, K., 2004. Thermal diffusivity and conductivity of olivine, wadsleyite and ringwoodite to 20 Gpa and 1373 K. Phys. Earth Planet. Inter. 143–144, 321–336.
Ziegler, P., Cloetingh, S., van Wees, J.-D., 1995. Dynamics of intraplate compressional deformation: the Alpine foreland and other examples. Tectonophysics 252, 7–59.
Ziegler, P., van Wees, J.-D., Cloetingh, S., 1998. Mechanical controls on collision related compressional intraplate deformation. Tectonophysics 300, 103–129.